Cellular/Molecular

Loss of miR-183/96 Alters Synaptic Strength via Presynaptic and Postsynaptic Mechanisms at a Central Synapse

Constanze Krohs,[1*] Christoph Körber,[2*] Lena Ebbers,[1] Faiza Altaf,[1] Giulia Hollje,[1] Simone Hoppe,[2] Yvette Dörflinger,[2] Haydn M. Prosser,[3] and Hans Gerd Nothwang[1,4]

[1]Division of Neurogenetics, Department of Neuroscience, Carl von Ossietzky University Oldenburg, Oldenburg 26129, Germany, [2]Institute of Anatomy und Cell Biology, Department of Functional Neuroanatomy, Heidelberg University, Heidelberg 69120, Germany, [3]Wellcome Trust Sanger Institute, Wellcome Trust Genome Campus, Cambridge CB10 1SA, United Kingdom, and [4]Excellence Cluster Hearing4all, Carl von Ossietzky University Oldenburg, 26129 Oldenburg, Germany

A point mutation in miR-96 causes non-syndromic progressive peripheral hearing loss and alters structure and physiology of the central auditory system. To gain further insight into the functions of microRNAs (miRNAs) within the central auditory system, we investigated constitutive *Mir-183/96*^{dko} mice of both sexes. In this mouse model, the genomically clustered miR-183 and miR-96 are constitutively deleted. It shows significantly and specifically reduced volumes of auditory hindbrain nuclei, because of decreases in cell number and soma size. Electrophysiological analysis of the calyx of Held synapse in the medial nucleus of the trapezoid body (MNTB) demonstrated strongly altered synaptic transmission in young-adult mice. We observed an increase in quantal content and readily releasable vesicle pool size in the presynapse while the overall morphology of the calyx was unchanged. Detailed analysis of the active zones (AZs) revealed differences in its molecular composition and synaptic vesicle (SV) distribution. Postsynaptically, altered clustering and increased synaptic abundancy of the AMPA receptor subunit GluA1 was observed resulting in an increase in quantal amplitude. Together, these presynaptic and postsynaptic alterations led to a 2-fold increase of the evoked excitatory postsynaptic currents in MNTB neurons. None of these changes were observed in deaf *Cldn14*^{ko} mice, confirming an on-site role of miR-183 and miR-96 in the auditory hindbrain. Our data suggest that the *Mir-183/96* cluster plays a key role for proper synaptic transmission at the calyx of Held and for the development of the auditory hindbrain.

Key words: **auditory hindbrain; calyx of Held; micro-RNA; synaptic transmission**

Significance Statement

The calyx of Held is the outstanding model system to study basic synaptic physiology. Yet, genetic factors driving its morphologic and functional maturation are largely unknown. Here, we identify the *Mir-183/96* cluster as an important factor to regulate its synaptic strength. Presynaptically, *Mir-183/96*^{dko} calyces show an increase in release-ready synaptic vesicles (SVs), quantal content and abundance of the proteins Bassoon and Piccolo. Postsynaptically, the quantal size as well as number and size of GluA1 puncta were increased. The two microRNAs (miRNAs) are thus attractive candidates for regulation of synaptic maturation and long-term adaptations to sound levels. Moreover, the different phenotypic outcomes of different types of mutations in the *Mir-183* cluster corroborate the requirement of mutation-tailored therapies in patients with hearing loss.

Received Jan. 16, 2020; revised May 3, 2021; accepted May 9, 2021.

Author contributions: C.Kr., C.Kö., L.E., H.M.P., and H.G.N. designed research; C.Kr., C.Kö., L.E., F.A., G.H., S.H., and Y.D. performed research; C.Kr., C.Kö., L.E., F.A., and G.H. analyzed data; C.Kr., C.Kö., and L.E. wrote the paper.

This work was supported by the Deutsche Forschungsgemeinschaft (DFG) Graduate School "Molecular Basis of Sensory Biology" Grant DFG GRK 1885 (to C.Kr., F.A., and H.G.N.), the DFG Grant SPP 1608 "Ultrafast and Temporally Precise Information Processing: Normal and Dysfunctional Hearing" (to C.Kö.), and the German Israeli Foundation "Function of microRNAs in the peripheral and central auditory system" GIF Grant I-1430-415.13/2017 (to H.G.N.). We thank the Developmental Studies Hybridoma Bank/Iowa for kindly providing antibodies and Prof. Dr. Michael Winklhofer for support regarding statistics. We also thank Martina Reents, Laura Rogge, and Marion Schmitt for excellent technical assistance and the Fluorescence Microscopy Service Unit, Carl von Ossietzky University of Oldenburg, for the use of the imaging facilities.

*C.Kr. and C.Kö. contributed equally to this work.

The authors declare no competing financial interests.

Correspondence should be addressed to Hans Gerd Nothwang at hans.g.nothwang@uni-oldenburg.de.

https://doi.org/10.1523/JNEUROSCI.0139-20.2021

Introduction

Development and function of the nervous system are shaped by a rich repertoire of genetic factors. Among them, microRNAs (miRNAs), a type of small non-coding RNAs, play key roles in the posttranscriptional regulation of gene expression by facilitating sequence-specific RNA interference. Mediated by Argonaute proteins and other components of RNA-induced silencing complex (RISC), miRNAs bind complementary sequences within mRNA transcripts. This results in decreased expression levels of target proteins. The binding has however not to be perfect across the entire mature miRNA sequence. In mammals, binding is dominated by the so-called seed region at the 5′ end, which consists of seven nucleotides (Lewis et al., 2003; Banks et al., 2020).

In humans, >2300 miRNAs have been identified (Alles et al., 2019), with each miRNA possibly contributing to the regulation of hundreds of target proteins (Lewis et al., 2016; Bartel, 2018). It is therefore estimated that >60% of vertebrate protein-coding mRNAs are regulated by miRNAs. In that manner, miRNAs possibly regulate all cellular processes in the nervous system (Friedman et al., 2009).

In the auditory system, miR-96 has emerged as a key factor for proper development and physiological activity (Banks et al., 2020). This miRNA is a member of the evolutionary highly conserved miRNA-183 cluster, which consists of miR-183, miR-96, and miR-182. Mutations in the seed region of *Mir-96* cause deafness both in men and mice (Lewis et al., 2009; Mencía et al., 2009; Kuhn et al., 2011; Soldà et al., 2012), because of hair cell degeneration. Analysis of the deaf *Diminuendo* (*Dmdo*) mouse model harboring a point mutation in the *Mir-96* seed region identified an additional broad spectrum of alterations in the auditory hindbrain. This included postnatal cell loss, reduced abundance of K^+-channels, as well as an immature calyx of Held synapse (Schlüter et al., 2018).

The calyx of Held is a giant glutamatergic, axosomatic synapse formed by the axons of the globular bushy cells in the ventral cochlear nucleus (VCN) onto the principal cells of the contralateral medial nucleus of the trapezoid body (MNTB) within the superior olivary complex (SOC). The synapse is specialized for high fidelity neurotransmission by harboring several hundred presynaptic active zones (AZs), which are equipped with a readily releasable pool (RRP) of thousands of synaptic vesicles (SVs; Sätzler et al., 2002; Taschenberger et al., 2002). On the postsynaptic site, the composition of AMPA receptors (AMPAR) is optimized to ensure rapid channel gating and provides large EPSCs (Yang et al., 2011; Borst and van Soria Hoeve, 2012). In stark contrast to the extensive knowledge of the physiological mechanisms underlying neurotransmission in this model system, genetic factors that drive its development and function are largely unknown. The neural recognition molecule NB-2 is involved in the initial formation of contacts between the axon and MNTB neurons (Toyoshima et al., 2009), and mice lacking bone morphogenic protein (BMP) receptors show small calyces with less mature transmitter release properties (Xiao et al., 2013). The immature state of the calyx of Held in homozygous *Dmdo* mice identified miR-96 as a further key molecule in shaping the calyx of Held synapse (Schlüter et al., 2018). To gain further insights into the role of miRNAs at the calyx of Held, we made use of a constitutive, deaf *Mir-183/96*^{dko} mouse (Lewis et al., 2021). We used this double knockout (dko) mouse since the polycistronic nature of the *Mir-183* cluster with only 117 nucleotides of intergenic region between *Mir-183* and *Mir-96* (Dambal et al., 2015) rendered genetic ablation of miR-96 alone on the DNA level technically difficult (Lewis et al., 2021). Morphologic and electrophysiological analysis revealed that miR-96 and miR-183 are involved in shaping synaptic transmission at the calyx of Held on the presynaptic and postsynaptic site, demonstrating that both miRNAs play a critical role in shaping synaptic transmission at a central synapse in the auditory brainstem.

Materials and Methods

Experimental design

Constitutive *Mir-183/96*^{dko} mice and their wild-type (wt) littermates were used to identify morphologic, electrophysiological, and molecular differences at the calyx of Held synapse. Because of the polycistronic structure of the miR-183 cluster with only 117 nucleotides between miR-183 and miR-96 (Dambal et al., 2015) genetic ablation of miR-96 is technically challenging to achieve (Lewis et al., 2021). We therefore used an animal model with the two closely related miR-183 and miR-96 being deleted. Despite high sequence homology between these two miRNAs, there are small differences in their sequences such as one nucleotide exchange in the seed region (Banks et al., 2020). This will result in regulation of common and unique mRNA targets, with distinct mRNA targets often within the same functional gene family (Dambal et al., 2015). We can therefore not unequivocally assign observed phenotypes in our mouse model to either of the two miRNAs. Since *Mir-183/96*^{dko} mice are deaf (Lewis et al., 2021), peripherally deaf *Claudin14* knockout *Cldn14*^{ko} mice were used in some experiments to control for possible effects arising from peripheral deafness (Ben-Yosef et al., 2003).

Animals

Mir-183/96^{dko} mice (C57BL/6N background; Prosser et al., 2011) or *Cldn14*^{ko} mice (NMRI background; Ben-Yosef et al., 2003) and their respective wt littermates of both sexes were used throughout the experiments. Protocols were approved by the local authorities (LAVES, Oldenburg; Regierungspräsidium Karlsruhe). All experiments were performed in accordance with the regulations of German federal law on the care and use of laboratory animals and followed the guidelines of the EU Directive 2010/63/EU for animal experiments.

Anatomical analysis of auditory brainstem nuclei

Mir-183/96^{dko} mice and wildtype (wt) littermates at the age of postnatal day (P)0, P25–P27, or P60 were injected intraperitoneally with a lethal dose of sodium pentobarbital (Narcoren, Merial; 650 mg/kg bodyweight) and perfused transcardially with PBS (136.9 mM NaCl, 2.7 mM KCl, 10.1 mM Na_2HPO_4, and 1.8 mM KH_2PO_4, pH 7.4) followed by 4% paraformaldehyde (PFA; 4% PFA in PBS, pH 7.4). Brains were postfixed in 4% PFA overnight and incubated for at least 16 h in 30% sucrose in PBS for cryoprotection. Brains were embedded in tissue freezing medium and stored at −80°C; 30-µm-thick coronal consecutive serial sections were cut on a cryostat (Leica Biosystems) using gelatin-chromalaun-coated slides and stored at −80°C. Only complete series of auditory brainstem sections from the beginning of the dorsal cochlear nucleus (DCN) to the end of the reticulotegmental nucleus (RtTg; seen from caudal) were used for subsequent Nissl staining and analysis of the volume of brainstem nuclei. Every section was imaged and digitalized with an automated bright field microscope (AxioScan Z1, Carl Zeiss). The volume of each nucleus was calculated by multiplying its manually outlined area with the thickness of each section (Hirtz et al., 2011; Schlüter et al., 2018). For determination of cell numbers at P0 and P 60, cells were marked and counted manually in ImageJ. The cross-section area (soma size) of cells at P60 was analyzed in 120 cells per nucleus (60 cells from the left and right side each) per animal. Cells were randomly chosen, the cell border was manually delineated and the area was calculated because of the known image dimensions by ImageJ.

Immunohistochemistry

At P30, mice were injected intraperitoneally with a lethal dose of sodium pentobarbital (Narcoren, Merial; 650 mg/kg bodyweight) and transcardially perfused with PBS followed by Zamboni solution (15% picric acid saturated H_2O, 2% PFA in PBS). Brains were postfixed in Zamboni solution for 3–4 h and incubated for at least 16 h in cryoprotection solution (30% sucrose in PBS); 30-µm-thick coronal sections of the auditory brainstem were cut on a sliding microtome (HM 430, Microm, Thermo Scientific) and stored in PBS at 4°C. Selected slices of the auditory brainstem were washed three times for 5 min in PBS followed by a 30 min wash in blocking solution (2% BSA, 0.3% Triton X-100, 10% goat serum in PBS). The sections were incubated over night at 4°C with the primary antibody diluted to the appropriate concentration in carrier solution (1% BSA, 0,3% Triton X-100, 1% goat serum in PBS). Primary antibodies and their dilutions in this study were: anti-Bassoon, monoclonal mouse, 1:200 (catalog #SAP7F407, Enzo Life Sciences); anti-GluA1, monoclonal mouse, 1:500 (catalog #182011, Synaptic Systems); anti-Homer1b/c, polyclonal rabbit, 1:500 (catalog #160023, Synaptic Systems); anti-Piccolo, polyclonal guinea pig, 1:200 (catalog #142104, Synaptic Systems); and anti-SV2, monoclonal mouse, 1:500 (DSHB). After washing the sections

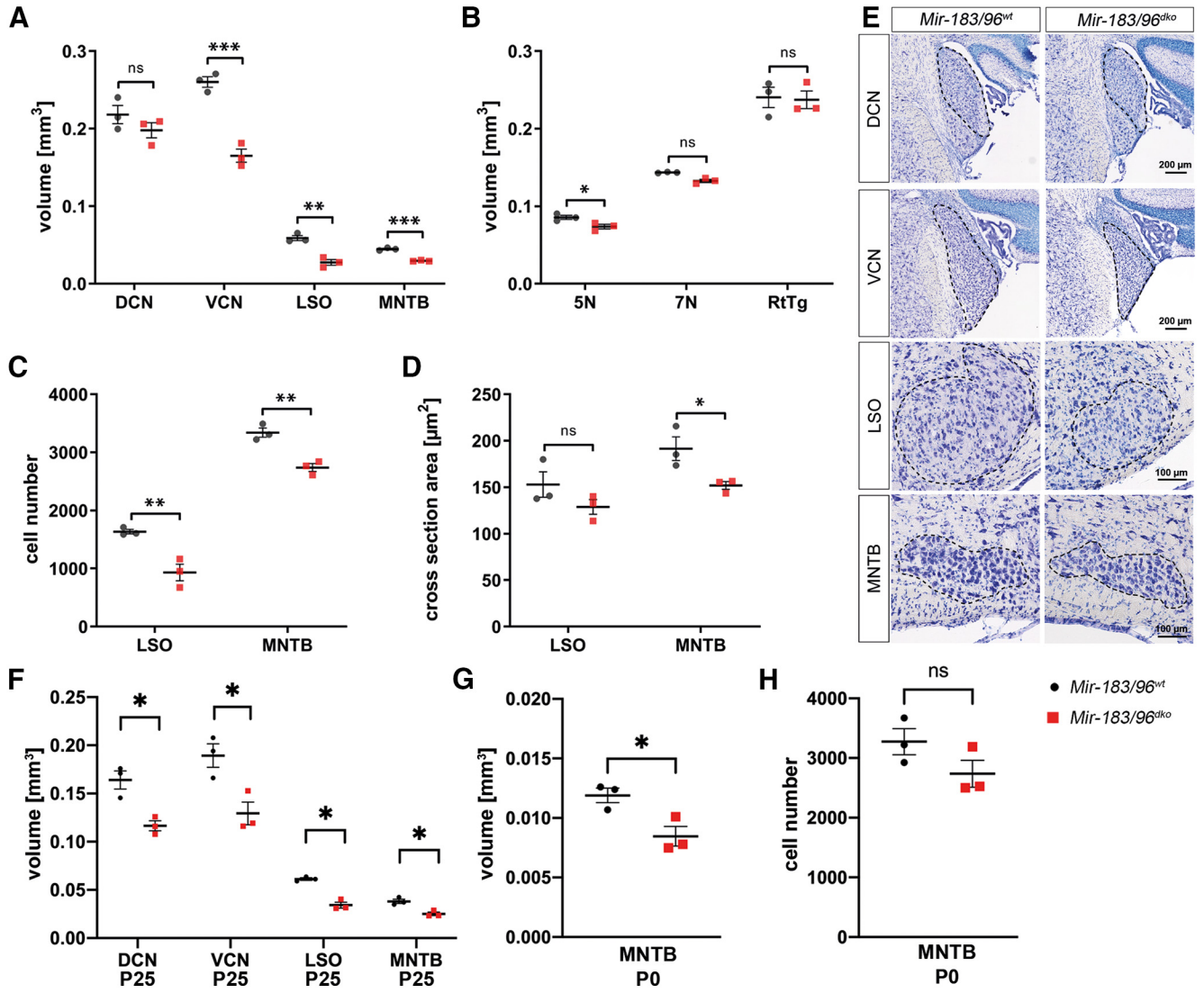

Figure 1. Significantly reduced volumes of auditory brainstem nuclei in *Mir-183/96*^{dko} mice. ***A***, ***B***, Quantification of the volumes of auditory (***A***) and non-auditory (***B***) brainstem nuclei in *Mir-183/96*^{dko} mice and wt littermates at P60. ***C***, Quantification of the number of neurons in the LSO and the MNTB of *Mir-183/96*^{dko} mice and wt littermates at P60. ***D***, Quantification of the neuron size in the LSO and the MNTB of *Mir-183/96*^{dko} mice and wt littermates at P60. ***E***, Representative Nissl images of the examined auditory brainstem nuclei at P60. ***F***, Quantification of the volumes of auditory brainstem nuclei in *Mir-183/96*^{dko} mice and wt littermates at P25–P27. ***G***, Morphometric analysis of the MNTB at P0 revealed a significant volume loss at birth. ***H***, Quantification of the cell number in the MNTB at P0. $n = 3$ mice/genotype. 5N, trigeminal motor nucleus; 7N, facial nucleus; DCN, dorsal cochlear nucleus; LSO, lateral superior olive; MNTB, medial nucleus of the trapezoid body; RtTg, reticulotegmental nucleus; VCN, ventral cochlear nucleus, these abbrevations apply to all other figures and tables as well. $n = 3$ mice/genotype. In ***D***, 120 cells/animal. Statistics for ***A***, ***B***: MANOVA; in ***C***, ***D***, ***G***, ***H***: Student's *t* test; in ***F***: Welch test with FDR correction. $^{*}p < 0.05$, $^{**}p < 0.01$, $^{***}p < 0.001$. ns = not significant.

three times for 5 min in PBS, they were incubated in a 1:1000 dilution of secondary antibody in carrier solution in the dark for 1.5 h at room temperature. Secondary antibodies used in this study were: Alexa Fluor (AF) 488 goat anti-mouse, catalog #A-11001, AF 488 goat anti-rabbit, catalog #A-11008; AF 647 goat anti-guinea pig, catalog #A-21450; AF 647 goat anti-chicken, catalog #A-21449; and AF 647 goat anti-rabbit, catalog #A-21244, all from Invitrogen. Thereafter, sections were washed three times in PBS in the dark, attached to gelatin-chromalaun-coated slides and air-dried. Sections on the slides were mounted with Mowiol supplemented with DAPI. Negative controls were conducted by omitting the primary antibody using only the secondary antibody on respective tissues. If available, preadsorption control experiments were performed and provided no signal above background (data not shown). Immunolabelling was examined in small confocal image stacks (largest cell diameter and the two adjacent optical sections) obtained from brainstem sections using a Leica TCS SP8 confocal laser scanning microscope equipped with a Leica HC PL APO 63×/1.4 oil objective. Image processing and analysis were performed using ImageJ.

Preparation of acute brainstem slices for electrophysiology

Mice of either genotype were rapidly decapitated at P25–P27. Brains were removed in ice-cold slicing solution containing the following: 125 mM NaCl, 25 mM $NaHCO_3$, 2.5 mM KCl, 1.25 mM NaH_2PO_4, 3 mM myoinositol, 2 mM Na-pyruvate, 0.4 mM ascorbic acid, 0.1 mM $CaCl_2$, 3 mM $MgCl_2$, and 25 mM glucose aerated with carbogen (5% CO_2 in O_2). Coronal slices of the auditory brainstem (250 µm thick) were prepared on a vibratome (VT1200S, Leica) and stored in ASCF containing the following: 125 mM NaCl, 25 mM $NaHCO_3$, 2.5 mM KCl, 1.25 mM NaH_2PO_4, 2 mM $CaCl_2$, 1 mM $MgCl_2$, and 25 mM glucose aerated with carbogen (pH 7.3) at 37°C for 45 min and at room temperature (22 ± 1°C) thereafter.

Electrophysiology

Whole-cell patch-clamp recordings from MNTB principal neurons were performed at room temperature in artificial CSF (ACSF) using an EPC-10/2 amplifier controlled by PatchMaster software (HEKA). Pipettes with open tip resistances of 2–3 MΩ were pulled from thick-walled borosilicate glass (catalog #1807515, Hilgenberg) and filled with pipette

Table 1. Morphometric analysis of *mir-183/96*^{dko} and corresponding wt animals

Parameter	*Mir-183/96*^{wt}	*Mir-183/96*^{dko}	*p* value	Cohens *d*
Volume auditory nuclei P60 (mm^3)				
n	3	3		
DCN	0.22 ± 0.012	0.198 ± 0.010	0.26	
VCN	0.26 ± 0.0068	0.165 ± 0.0086	0.00096	−7.069
LSO	0.059 ± 0.0032	0.028 ± 0.0037	0.0030	−5.387
MNTB	0.045 ± 0.0010	0.030 ± 0.0004	0.00016	−11.22
Volume non-auditory nuclei P60 (mm^3)				
n	3	3		
5N	0.086 ± 0.0026	0.074 ± 0.0029	0.039	−2.667
7N	0.14 ± 0.00038	0.13 ± 0.0020	0.065	
RtTg	0.24 ± 0.013	0.24 ± 0.011	0.87	
Brain size P60 (g)				
n	3	3		
brain weight	0.47 ± 0.0047	0.42 ± 0.0081	0.0022	−7.551
Cell number P60				
n	3	3		
LSO	1635.42 ± 38.12	931.67 ± 141.75	0.0087	−3.92
MNTB	3341.58 ± 79.52	2739.92 ± 67.98	0.0045	−4.70
Cell size P60 (μm^2)				
n	120	120		
LSO	152.89 ± 13.63	128.89 ± 7.89	0.20	
MNTB	191.58 ± 12.60	151.92 ± 4.16	0.040	−2.44
Volume auditory nuclei P25–P27 (mm^3)				
n	3	3		
DCN	0.164 ± 0.0094	0.117 ± 0.0052	0.0263	−3.61
VCN	0.186 ± 0.0122	0.129 ± 0.0203	0.0263	−2.74
LSO	0.061 ± 0.0013	0.034 ± 0.0030	0.013	−6.66
MNTB	0.038 ± 0.0022	0.025 ± 0.0019	0.0239	−3.65
Volume auditory nuclei P0 (mm^3)				
n	3	3		
MNTB	0.0119 ± 0.0006	0.0085 ± 0.0008	0.028	−2.75
Cell number P0				
n	3	3		
MNTB	3274 ± 217.4	2738 ± 225.1	0.162	

Data are shown as mean ± SEM.

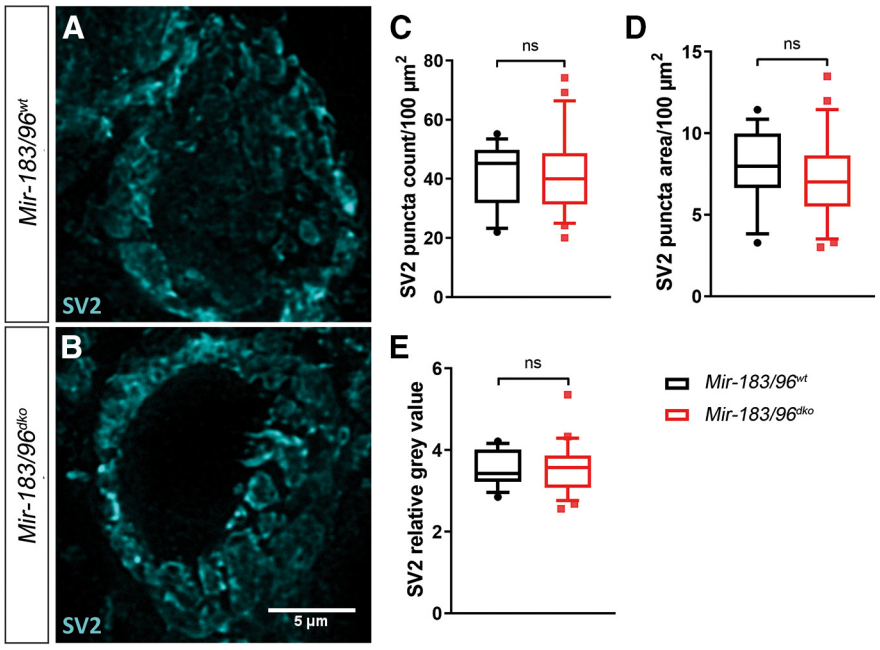

Figure 2. No changes in SV2 expression in the calyx of Held of *Mir-183/96*^{dko} mice. ***A***, ***B***, Representative images showing immunohistochemical labeling of SV2 in single calyx of Held terminals at P30. ***C–E***, Quantification of the number (***C***) and area (***D***) of SV2 puncta/100 μm^2 as well as the relative gray value measurements of SV2 immunoreactivity. $N = 45$ cells from 3 animals per genotype. Statistics: Student's *t* test. ns = not significant.

solution containing the following: 130 mM Cs gluconate, 10 mM CsCl, 10 mM HEPES, 10 mM TEA-Cl, 5 mM Na_2- mM phosphocreatine, 5 mM EGTA, 4 mM Mg-ATP, and 0.3 mM GTP (pH 7.2). The membrane potential was set to −70 mV and the series resistance (3–6 MΩ) was compensated by >90%. Currents were digitized at 20–100 kHz and Bessel-filtered (2.9 kHz). Synaptic release from the calyx of Held was evoked by afferent fiber stimulation via a parallel bipolar electrode (FHC) placed close to midline (2- to 6-V stimuli, 70–100 μs in duration). Spontaneous EPSCs (sEPSCs), which are equivalent to mEPSC at the calyx of Held synapse (Ishikawa et al., 2002), were identified based on their fast kinetics (decay time constant <1.5 ms). sEPSC amplitude and kinetics recorded from wt mice are in good agreement with previously published data (Taschenberger et al., 2005), indicating that a mis-assignment of a significant proportion of mIPSCs as sEPSCs is highly unlikely. In some recordings, ACSF was supplemented with 1 mM kynurenic acid (Kyn; Abcam). sEPSC amplitudes in ACSF supplemented with 1 mM Kyn were calculated assuming a similar decrease in amplitude for sEPSCs and evoked EPSCs, as described previously (Neher and Sakaba, 2001). This was necessary, since the reduction in sEPSC

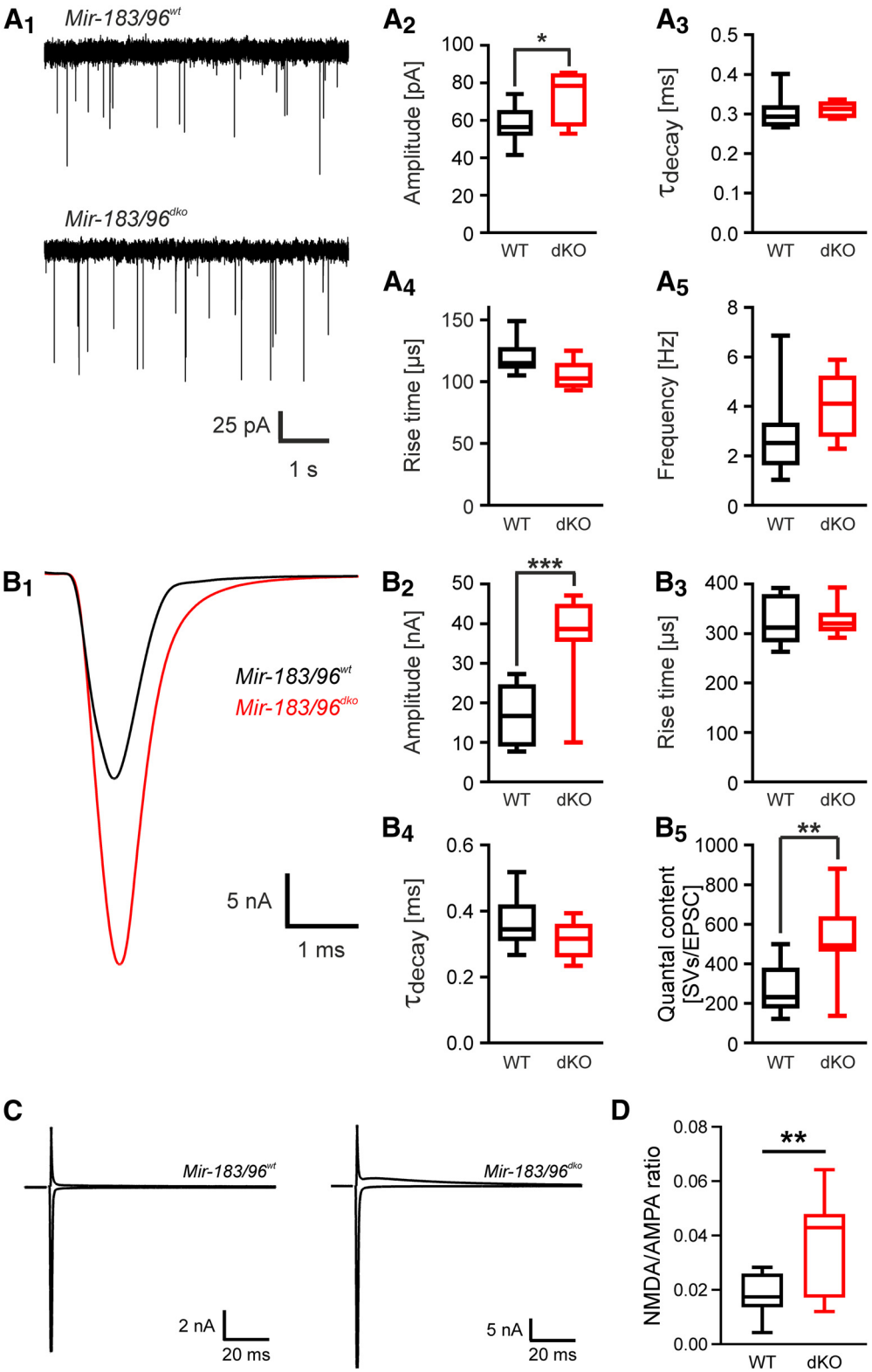

Figure 3. Increased spontaneous and evoked synaptic transmission at the calyx of Held in *Mir-183/96*^{dko} mice. ***A***, Representative sample current traces of sEPSCs (***A1***) and quantification of spontaneous release parameters (amplitude, frequency, and kinetics; ***A2–A5***). ***B***, Representative sample current traces of evoked EPSCs (***B1***) and quantification of evoked release parameters (amplitude, kinetics, and quantal content; ***B2–B5***). ***C***, Representative current responses recorded at holding potentials of −70 mV (AMPARs) and +40 mV (NMDARs) from wt and *Mir-183/96*^{dko} calyces. ***D***, Quantification of the ratios between the NMDAR-mediated and AMPAR-mediated current components. sEPSCs: $N = 6$ (wt), 9 (dko) synapses. eEPSCs: 10 (wt), 12 (dko) synapses. NMDA/AMPA ratio: $N = 9$ (dko), 13 (wt). Results were obtained from at least three animals/genotype. EPSC, excitatory postsynaptic current; SVs, synaptic vesicles. Statistics: Student's *t* test. $^{*}p < 0.05$, $^{**}p < 0.01$, $^{***}p < 0.001$.

amplitude may have caused a large fraction of sEPSCs to vanish in the noise, thereby preventing us from accurately measuring their amplitude. NMDA/AMPA ratios were determined in ASCF supplemented with strychnine (2 μM, Abcam) and gabazine (SR95531, 10 μM, Abcam) to block glycine and GABA receptors, respectively. AMPA receptor mediated currents were recorded at a holding potential of −70 mV, whereas NMDA receptor (NMDAR)-mediated currents were detected as a second release component at a holding potential of +40 mV.

Data were analyzed using custom-written IGOR (Wavemetrics) routines.

Electron microscopy

Tissue preparation, processing and scanning electron microscopy were performed as described previously (Horstmann et al., 2012). In brief, animals (P25–P27) were deeply anaesthetized and transcardially perfused with PBS followed by 4% PFA dissolved in PBS. Brains were removed and stored in fixative overnight. Coronal brainstem slices (100 µm) were prepared on a vibratome (Sigmann Elektronik) and incubated in cacodylic acid (100 mM) for 30 min. The MNTB was excised and postfixed in 1.5% potassium ferrocyanide and 2% osmium tetroxide (1 h, on ice). Samples were washed (H_2O followed by PBS), dehydrated in an ascending series of alcohol, incubated in propylenoxide/epoxy (1:1) over night and embedded in epoxy resin (polymerization: 36 h, 60° C). Ultrathin sections (40 nm) through the MNTB were cut on an Ultracut S microtome (Leica) equipped with a diamond knife angled at 45° (Diatome) and collected on clean, hydrophilized silicon wafers (SiMat Silicon Materials). The sections were exposed to chloroform vapor, to neutralize tissue compression because of sectioning, and stained using the modified Reynolds-procedure [saturated uranyl acetate (16 min) followed by lead citrate (8 min)]. Scanning electron microscopy was performed on a LEO Gemini 1530 equipped with a field emission gun and an ATLAS scanning generator (Zeiss). Images were taken at a pixel size of 3.8 nm using either the SE2 (4.6-mm working distance, 30-μm aperture, 2-keV acceleration voltage) or the inlense detector (3.6-mm working distance, 30-μm aperture, 2-keV acceleration voltage). Electron microscopy experiments and analysis were performed in a double-blind manner, i.e., neither the experimenter nor the analyzer were aware of the animal's genotype. Electron micrographs were taken from 8 to 10 randomly selected calyces per animal. AZs and SVs were manually traced using OpenCAR software (Sätzler et al., 2002). AZs were identified by the presence of an opposing postsynaptic density (PSD) and of SVs in the vicinity. The later criterion was necessary to discriminate AZs from puncta adherentia (Sätzler et al., 2002). The perpendicular distance between individual SVs and the AZ was calculated using OpenCARe and corrected for the SV radius.

Statistical analysis

Statistical analysis was assigned by MANOVA (two groups, multiple parameters), one-way ANOVA followed by Sidak's multiple comparison *post hoc* test (more than two groups, one parameter) or Student's *t* test (two groups) using R or GraphPad Prism 8 software (GraphPad). Data were derived from at least three animals per genotype. The number of cells or synapses examined is indicated in tables and/or figure legends. In box plots, the box shows the median and the upper and lower quartile, while whiskers show the 5th–95th percentiles of each dataset. Data points laying outside this range are shown separately. Effect sizes are reported as Cohen's *d* for significant results. Significant *p* values are depicted with asterisks within in the quantification plots: $*p < 0.05$, $**p < 0.01$, $***p < 0.001$. ns = not significant. Quantitative data are always presented as mean ± SEM.

Results

Volume reduction of auditory brainstem nuclei in *mir-183/96*^{dko} mice

Homozygote *Dmdo* mice show significant volume reductions of auditory nuclei (Schlüter et al., 2018). We therefore investigated the anatomy of the auditory hindbrain of *Mir-183/96*^{dko} mice at P60 and P25 – 27 to assess whether loss of the two miRNAs has similar functional consequences. Quantitative analysis of Nissl-stained sections demonstrated that three out of four auditory nuclei, i.e., the VCN which is part of the cochlear nucleus complex (CNC), as well as the lateral superior olive (LSO) and MNTB of the SOC, displayed significant volume reductions at P60 (Fig. 1*A*,*E*; Table 1). The VCN volume was reduced by 36.5%. The LSO was even 53.2% smaller in *Mir-183/96*^{dko} animals. The MNTB displayed a volume reduction by 33.8%. In contrast, the DCN volume showed no significant volume reduction.

Table 2. Properties of calyx of Held synapses recorded in normal ACSF

Parameter	wt	*Mir-183/96*^{dko}	*p* value	Cohens *d*
sEPSC				
n	9	6		
Amplitude (pA)	56.2 ± 3.2	73.0 ± 5.7	0.0299	1.285
Rise time (µs)	120 ± 5	105 ± 5	0.0577	
τ_{decay} (ms)	0.302 ± 0.015	0.312 ± 0.020	0.6244	
Frequency (Hz)	2.87 ± 0.57	4.06 ± 0.57	0.1809	
eEPSC				
n	10	12		
Amplitude (nA)	16.81 ± 2.32	36.10 ± 3.41	0.0002	0.794
Rise time (µs)	322 ± 15	327 ± 9	0.777	
τ_{decay} (ms)	0.363 ± 0.026	0.315 ± 0.018	0.1409	
Quantal content (SVs)	272 ± 39	507 ± 57	0.0041	1.392
STD (100 Hz)				
n	10	11		
τ (ms)	22.3 ± 4.3	19.3 ± 2.1	0.5182	
Depression (%)	90.2 ± 1.5	90.9 ± 0.9	0.6887	
PPR	0.57 ± 0.07	0.57 ± 0.05	0.9728	
Steady-state EPSC (nA)	1.70 ± 0.25	3.11 ± 0.43	0.0037	1.446
RRP				
n	10	11		
RRP size (nA)	53.49 ± 6.89	100.60 ± 11.86	0.0034	1.461
RRP size (SVs)	899 ± 79	1386 ± 156	0.0142	1.177
Replenishment rate (nA/ms)	0.177 ± 0.026	0.329 ± 0.035	0.0029	
Norm. repl. rate (ms^{-1})	0.012 ± 0.002	0.010 ± 0.001	0.3221	1.493
P_r	0.322 ± 0.034	0.367 ± 0.030	0.3436	
NMDA/AMPA ratio				
n	13	9		
NMDA/AMPA ratio	0.018 ± 0.002	0.035 ± 0.006	0.0064	1.319

Data are shown as mean ± SEM. eEPSC, evoked postsynaptic current; sEPSC, spontaneous postsynaptic current; RRP, readily releable pool; STD, short term depression.

To check for the impact on non-auditory structures, we also probed the trigeminal motor nucleus (5N), the facial nucleus (7N), and the RtTg at P60 (Fig. 1*B*; Table 1). The 5N was significantly (-13.9%) smaller, although the reduction was much less pronounced than in the auditory nuclei. The 7N and the RtTg were not reduced. The small reduction in 5N volume could be explained by a slight, but statistically significant general reduction in brain size at P60, as evidenced by a 10.6% reduction in brain weight in *Mir-183/96*^{dko} mice. We thus conclude that these non-auditory nuclei were not specifically affected by *Mir-183/96*^{dko} and therefore omitted them from further analyses.

To address the question, whether the volume reduction in the LSO and MNTB is because of a decrease in cell number or cell (soma) size, we quantified both parameters at P60 (Fig. 1*C*,*D*; Table 1). The LSO revealed a significant decrease of 43.0% in cell number, but no significant change in soma size. The MNTB showed significant decreases of 18.0% in cell number and 20.7% in cell soma size. These results reveal that the decreased volume of the LSO and MNTB is mainly because of fewer cells in the LSO and because of fewer and smaller cells in the MNTB.

A volume assessment at earlier ages (P25–P27) that match with the age of subsequent electrophysiological recordings revealed a similar volume loss of the auditory hindbrain. The only difference was the volume reduction in the DCN as it reached significance at this age (Fig. 1*F*; Table 1).

To frame the timeline of volume and cell loss in the hindbrain of *Mir-183/96*^{dko} mice, we assessed the cell number in the MNTB at P0. We focused on the MNTB as this nucleus is clearly identifiable at this early age. Already at birth, the MNTB displayed a

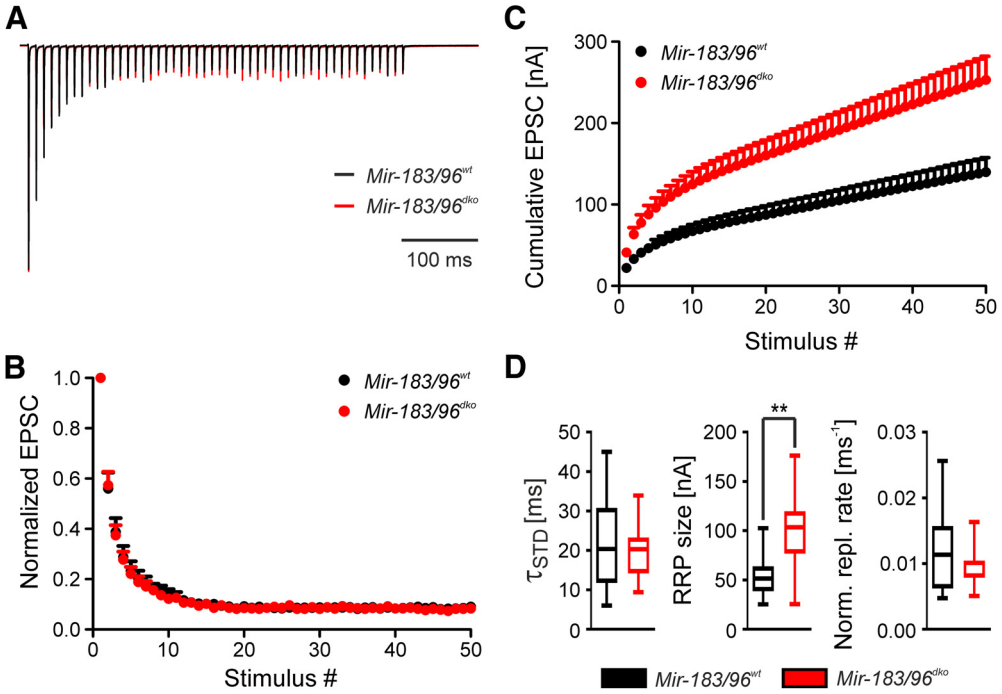

Figure 4. Knock-out of *Mir-183/96* has no effect on short-term plasticity but increases the RRP. ***A***, Superimposed scaled representative current traces recorded during 100-Hz stimulus trains (50 stimuli). ***B***, Averaged normalized EPSC amplitudes during 100-Hz trains. ***C***, Averaged cumulative EPSCs amplitudes during 100-Hz trains. ***D***, Quantification of the time constant of EPSC amplitude decay during 100-Hz trains (left), the RRP size (middle) and the replenishment rate normalized to the EPSC amplitude (right). $N = 10$ (wt), 11 (dko) synapses from at least three animals/genotype. EPSC, excitatory postsynaptic current. RRP, readily releable pool. Statistics: Student's *t* test. $^{**}p < 0.01$.

drastic volume loss of 28.9% (Fig. 1*G*; Table 1), whereas cell number was not significantly altered (Fig. 1*H*; Table 1). The combined loss of miR-183 and miR-96 thus affects the anatomy of auditory hindbrain structures earlier than in the *Dmdo* mouse. There, volume differences between wt and *Dmdo* mice started to occur between P0 and P4 (Schlüter et al., 2018). Our findings point to a requirement of miR-183 and miR-96 during embryonic development for proper auditory hindbrain formation.

Gross synaptic morphology of the calyx of Held is unchanged in *mir-183/96^{dko}* mice

Dmdo mutant mice show deficits in structural maturation of the calyx of Held synapse, i.e., the formation of distinct SV glycoprotein 2 (SV2) puncta (Schlüter et al., 2018). The latter probably reflects the fenestration of the synapse from a cup-like structure into stalks. Analysis of the distribution of SV2 immunoreactive puncta in P30 *Mir-183/96^{dko}* calyces showed no differences compared with wt littermates (Fig. 2*C*). We also measured the area of SV2 puncta (Fig. 2*D*) and quantified the relative immunoreactivity of SV2 (Fig. 2*E*). In all cases, we found no significant differences between genotypes. This suggests an unperturbed maturation of the calyx of Held in *Mir-183/96^{dko}* mice, which is in striking contrast to the immature phenotype seen in *Dmdo* mice (Schlüter et al., 2018).

Increased synaptic strength in *mir-183/96^{dko}*

We next sought out to examine the functional impact of miR-183/96 deficiency on synaptic transmission at the calyx of Held synapse. Therefore, we first recorded sEPSCs (equivalent to mEPSCs at the calyx of Held; Ishikawa et al., 2002) from MNTB principal neurons in acute brainstem slices prepared from *Mir-183/96^{dko}* mice and wt littermates at P25–P27. *Mir-183/96^{dko}* resulted in a 1.3-fold increase in sEPSC amplitudes, while leaving sEPSC kinetics and frequency unaffected (Fig. 3*A*; Table 2). This increase in sEPSC amplitude is not because of deafness, as it is not present in *Cldn14^{ko}* mice (Schlüter et al., 2018). To investigate whether the increase in sEPSC amplitude affects AP-driven synaptic transmission in *Mir-183/96^{dko}* mice, we recorded single EPSCs evoked from the calyx of Held at low frequency (0.1 Hz). In line with the results obtained for sEPSCs, we found EPSC amplitudes recorded from *Mir-183/96^{dko}* synapses to be approximately doubled with no changes in EPSC kinetics (Fig. 3*B1–B4*; Table 2). To distinguish whether the increase in EPSC amplitude was because of an increase in quantal amplitude (sEPSC amplitude), an increase in the number of vesicles released per EPSC, or a combination of both, we calculated the quantal content of the EPSCs. Taking into account the increased quantal amplitude, we still found *Mir-183/96^{dko}* calyces to release almost twice as many SVs per EPSCs as wt controls (Fig. 3*B5*; Table 2). The increase in quantal content argues against a purely postsynaptic effect to cause the increase in EPSC amplitude.

To gain insight into SV release during high-frequency synaptic transmission, we investigated EPSCs elicited by trains of high-frequency action potentials (APs) (50 stimuli at 100 Hz; Fig. 4*A*). We found prominent short-term depression (STD), a hallmark of the calyx (Borst et al., 1995; Taschenberger and von Gersdorff, 2000; Körber et al., 2015) both at wt and *Mir-183/96^{dko}* calyces. Moreover, STD was not different between the two genotypes in any of the parameters examined [time constant of EPSC amplitude decay, extent of depression, paired-pulse ratio (PPR); Fig. 4*A*,*B*,*D*; Table 2]. The only significant difference observed during high-frequency stimulation was an increase in the steady state EPSC amplitude during the late phase of the train (Fig. 4*A*; Table 2). Next, we investigated the size and dynamics of the RRP, employing the cumulative EPSC method (Schneggenburger et al., 1999; Fig. 4*C*). The RRP was twice as large in *Mir-183/96^{dko}* calyces as compared with wt controls (Fig.

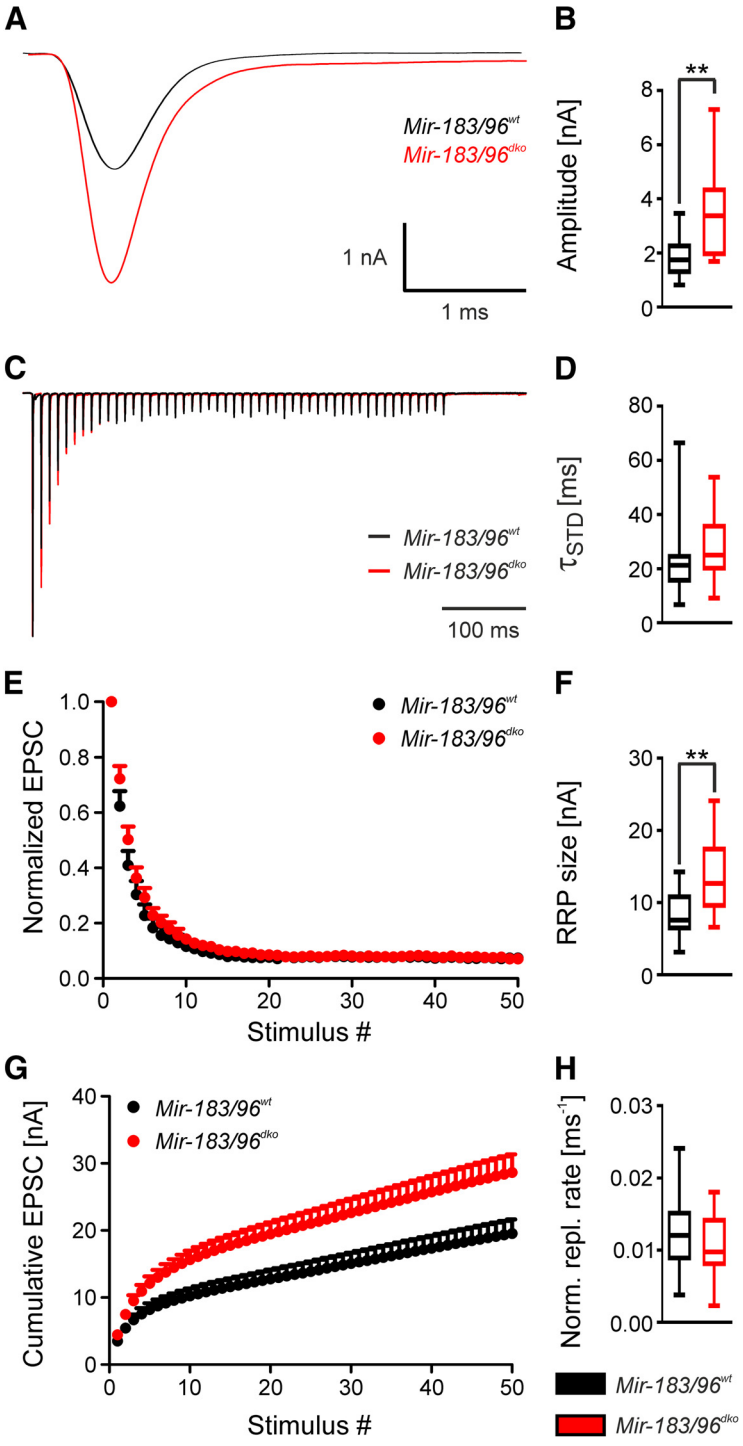

Figure 5. Increased evoked EPSC amplitude and RRP size in *Mir-183/96*^{dko} calyces are not because of AMPAR saturation since they persist in the presence of Kyn. ***A***, Representative sample current traces of evoked EPSCs. ***B***, Quantification of evoked EPSC amplitudes. ***C***, Superimposed scaled representative current traces recorded during 100-Hz stimulus trains (50 stimuli). ***D***, Quantification of the time constant of EPSC amplitude decay during 100-Hz trains. ***E***, Averaged normalized EPSC amplitudes during 100-Hz trains. ***F***, Quantification of the RRP size. ***G***, Averaged cumulative EPSCs amplitudes during 100-Hz trains. ***H***, Quantification of the replenishment rate normalized to the EPSC amplitude. *N* = 15 (wt), 18 (dko) synapses from at least three animals/genotype. *N* (dko) in ***B*** = 17. EPSC, excitatory postsynaptic current. Statistics: Student's *t* test. $^{**}p < 0.01$.

4*D*; Table 2). Even when we normalized the RRP to the sEPSC amplitude to account for the increase in quantal amplitude, we found the RRP of *Mir-183/96*^{dko} synapses to contain ~50% more SVs than wt ones (Table 2). The replenishment rate of the RRP appeared to be faster in *Mir-183/96*^{dko} calyces as well (Table 2). However, when we normalized the replenishment rate to the first EPSC in the train, to take into account the intrinsically high variance of EPSC amplitudes, we did not observe any significant difference anymore (Fig. 4*D*; Table 2). Thus, the apparent effect of miR-183/96 loss on the replenishment rate seems to be an adjustment to the increases in EPSC amplitude and RRP size. These results suggest that the increase in EPSC amplitude observed in *Mir-183/96*^{dko} calyces is caused by an increase in RRP size, as the vesicular probability of release (P_r) remained unaffected by the absence of miR-183/96 (Table 2).

The EPSCs recorded from *Mir-183/96*^{dko} synapses were very large and could have led to AMPAR saturation. To rule out possible effects of AMPAR saturation on our analysis, we repeated the experiments on AP-evoked EPSCs in the presence of 1 mM Kyn. Kyn is a partial AMPAR antagonist with fast off-kinetics that prevents AMPAR saturation (Traynelis et al., 2010). EPSCs, evoked at 0.1-Hz frequency, were increased in amplitude in *Mir-183/96*^{dko} synapses, reflecting an increase in quantal content as seen in the initial experiments performed in the absence of Kyn (Fig. 5; Table 3). Of note, we observed a slight slowing of the EPSC decay time constant (Table 3). STD in response to high-frequency stimulation remained unaffected by loss of miR-183/96 in the presence of Kyn (Fig. 5*D*; Table 3). However, the increase in steady state EPSC amplitude during the late phase of the train seen in the absence of Kyn, did not reach significance anymore ($p = 0.07$). This was probably because of the reduced absolute difference in values (Fig. 5; Table 3). Re-examination of RRP size and replenishment rate confirmed the results obtained previously, as we again detected an increase in RRP size, but not in replenishment rate in calyces from *Mir-183/96*^{dko} mice (Fig. 5*F*,*H*; Table 3). Taken together, this set of experiments confirms our interpretation that loss of miR-183/96 results in increases in quantal content and RRP size along with the quantal amplitude.

NMDARs persist at the calyx of Held synapse of *mir-183/96*^{dko} mice

The increase in EPSC amplitude, and thus synaptic strength, at *Mir-183/96*^{dko} calyces is in contrast to the unchanged EPSC amplitude in *Dmdo* calyces. However, *Dmdo* calyces show NMDAR-mediated currents at P25, in line with the arrest in synaptic maturation (Schlüter et al., 2018). To compare further the calyces of *Mir-183/96*^{dko} and *Dmdo* mice, we recorded NMDA/AMPA ratios at *Mir-183/96*^{dko} calyces. NMDAR-mediated and AMPAR-mediated currents were recorded at holding potentials of +40 and −70 mV, respectively. Current responses recorded in *Mir-183/96*^{dko} calyces at +40 mV showed a second component ~10 ms after stimulation,

Table 3. Properties of calyx of Held synapses recorded in ACSF supplemented with 1 mM Kyn

Parameter	wt	*Mir-183/96*^{dko}	*p* value	Cohens *d*
eEPSC				
n	15	17		
Amplitude (nA)	1.92 ± 0.21	3.33 ± 0.38	0.0037	1.114
Rise time (µs)	271 ± 5	285 ± 6	0.072	
τ_{decay} (ms)	0.308 ± 0.008	0.341 ± 0.012	0.0377	0.786
Quantal content (SVs)	289 ± 32	494 ± 56	0.0046	1.084
STD (100 Hz)				
n	15	18		
τ (ms)	22.1 ± 3.5	27.9 ± 2.7	0.1966	
Depression (%)	92.4 ± 0.9	91.9 ± 1.0	0.6764	
PPR	0.62 ± 0.06	0.72 ± 0.05	0.1775	
Steady-state EPSC (pA)	209 ± 25	285 ± 0.31	0.0742	
RRP				
n	15	18		
RRP size (nA)	8.47 ± 0.89	13.39 ± 1.17	0.0029	1.132
RRP size (SVs)	1278 ± 134	1987 ± 174	0.0038	1.096
Replenishment rate (nA/ms)	0.022 ± 0.003	0.032 ± 0.004	0.0526	
Norm. repl. rate (ms^{-1})	0.012 ± 0.001	0.011 ± 0.001	0.3147	
P_r	0.230 ± 0.012	0.241 ± 0.016	0.6007	

Data are shown as mean ± SEM. eEPSC, evoked postsynaptic current; RRP, readily releable pool; STD, short term depression.

indicative of NMDAR-mediated current responses (Forsythe and Barnes-Davies, 1993; Joshi and Wang, 2002; Schlüter et al., 2018) that was absent in wt calyces (Fig. 3*C*). Normalization of the NMDAR-mediated component to the AMPAR-mediated EPSC amplitude at −70 mV revealed a significant increase in the NMDA/AMPA ratio in *Mir-183/96*^{dko} calyces (Fig. 3*D*; Table 2). The increase in the NMDA/AMPA ratio at the calyx in both *Mir-183/96*^{dko} and *Dmdo* mice suggests that a loss of function of miR-96 prevents NMDAR downregulation during synaptic maturation.

Changes in AZ composition and ultrastructure at the calyx of Held in *mir-183/96*^{dko} mice

Having established an increase in the RRP in calyces of *Mir-183/96*^{dko} mice, we investigated whether this was accompanied by an increase in the number of AZs. Therefore, we performed immunolabeling and particle analysis of the AZ marker proteins Bassoon and Piccolo (Fig. 6*A–D*). We found no changes in the number of Bassoon and Piccolo puncta between *Mir-183/96*^{dko} and wt calyces (Fig. 6*B*; Table 4). However, the mean size of puncta was significantly increased in *Mir-183/96*^{dko} mice by 7.1% for Bassoon and 29% for Piccolo when compared with wt (Fig. 6*C*; Table 4). Along the same lines, the quantification of the relative intensity of the immunoreactivity revealed an increase of 12.1% for Piccolo in *Mir-183/96*^{dko} mice, but not for Bassoon (Fig. 6*D*; Table 4).

To control for effects caused by deafness, we included the peripherally deaf *Cldn14*^{ko} mouse as further control (Fig. 6*A–D*; Table 4). We did neither observe significant changes in Piccolo and Bassoon puncta number and size in *Cld14*^{ko} mice, as compared with the respective wt controls, nor in relative immunoreactivity. Comparison of *Mir-183/96*^{dko} synapses to *Cldn14*^{ko} ones revealed also significant changes in mean puncta sizes of Bassoon (Table 4). These findings suggest that loss of miR-183/96 does not lead to the formation of additional AZs, but rather the resulting ones are larger or contain at least higher amounts of Bassoon and Piccolo.

We next investigated the ultrastructure of wt and *Mir-183/96*^{dko} AZs at P25 by scanning electron microscopy. AZs were identified in electron micrographs by the presence of a PSD and SVs in its vicinity (Fig. 7*A*). Ultrastructurally, AZs from wt and *Mir-183/96*^{dko} mice did not differ in AZ length or SV diameter (Fig. 7*A*,*C*; Table 4). However, when we analyzed the distances of the SVs to the AZ, we found more SVs in the immediate vicinity of the AZ (0- to 20-nm distance) in *Mir-183/96*^{dko} calyces as compared with wt ones (Fig. 7*B*,*C*; Table 4). We calculated the average number of SVs close to the AZ (0–20 nm) per AZ and again found increased SV numbers in *Mir-183/96*^{dko} calyces (Fig. 7*C*; Table 4). Since the SVs close to the AZ are thought to compromise the RRP (Imig et al., 2014), the increase in SVs close to the AZ in *Mir-183/96*^{dko} calyces is in line with our electrophysiological results showing an increase in RRP size. Interestingly, we observed fewer SVs at greater distances from the AZ (200–240 nm; Fig. 9*B*) in *Mir-183/96*^{dko} calyces. Although this change is small, it may indicate a general shift in SV distribution toward the AZ. Taken together, *Mir-183/96*^{dko} calyces show larger and more intense immune signals for Bassoon and Piccolo but no changes in AZ length, indicating rather an altered molecular composition of the cytomatrix of the AZ rather than an increase in size. However, ultrastructural analysis revealed an increase in SVs close to the AZ, indicative of an enlarged RRP and thus an altered SV distribution in *Mir-183/96*^{dko} calyces.

Increased number and size of synaptic GluA1 clusters in *mir-183/96*^{dko} mice

The alterations at the AZ described so far do not explain the increase in sEPSC amplitude. However, the AMPAR subunit GluA1 is a known target of miR-96 (Jensen and Covault, 2011; Dambal et al., 2015). We thus investigated whether loss of mir-183/96 had an effect on the expression level of GluA1 and, more important, its localization to the PSD. Therefore, we analyzed the abundance of GluA1 in the MNTB principal cell and its synaptic localization by means of immunohistochemistry (Fig. 8*A–D*). We found GluA1 particles to form larger clusters in the cell interior in *Mir-183/96*^{dko} mice as compared with wt littermates (Fig. 8*A*,*B*). Quantification of number and mean size of GluA1 puncta larger than 0.01 µm^2 resulted in a doubling in the number of these large GluA1 puncta in *Mir-183/96*^{dko} mice, as compared with wt littermates (Fig. 8*C*; Table 4). Moreover, we observed a strong increase in the average size of these large puncta by 57.7 (Fig. 8*D*; Table 4). Notably, the relative gray value analysis did not reveal differences in the overall immunoreactivity for GluA1 (data not shown).

In *Cldn14*^{ko} mice, the number of GluA1 puncta larger than 0.01 µm^2 and their mean size were unchanged compared with the respective wt littermates (Table 4) GluA1 puncta count was ~2.5 times higher in *Mir-183/96*^{dko} synapses compared with the *Cldn14*^{ko} ones, which was highly significant (Table 4). This also holds true for comparison of the mean puncta size, which was twice as large in the *Mir-183/96*^{dko} calyx compared with the *Cldn14*^{ko} synapse (Table 4).

To investigate whether the increase in number and size of GluA1 puncta led to a stronger incorporation of GluA1 subunits into the postsynaptic receptor complexes, we first examined the co-localization of GluA1 with the PSD marker Homer 1. We defined those puncta as co-localized that showed at least 1% overlap in small confocal image stacks. The number of GluA1 puncta co-localized with Homer 1 was increased in *Mir-183/96*^{dko} synapses (Fig. 8*D*,*E*; Table 4). However, we realized that the total area of Homer 1 puncta was enlarged, too (Fig. 8*E*; Table 4). Indeed, Homer 1 is a validated target of miR-96 (Dambal et al., 2015), which explains the increase in area in

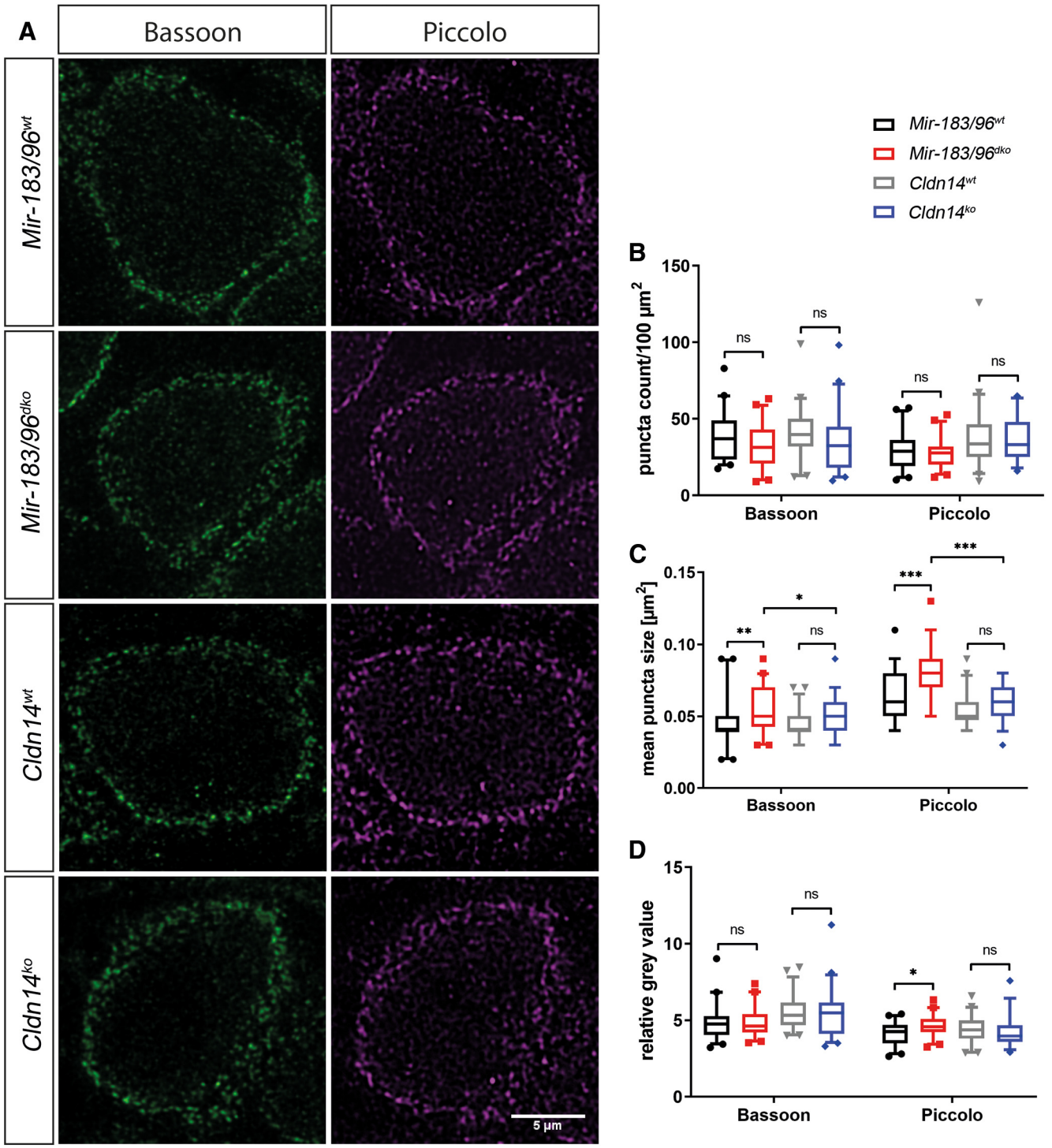

Figure 6. Increased puncta size of the presynaptic proteins Bassoon and Piccolo in *Mir-183/96*^{dko} mice. ***A***, Representative images showing immunohistochemical labeling of Bassoon and Piccolo in *miR-183/96* wt and ko calyces as well as in *Cldn14* wt and ko synapses. ***B–D***, Quantification of the number (***B***) and size (***C***) of Bassoon and Piccolo puncta as well as the relative gray value measurements of Bassoon and Piccolo immunoreactivity. $N = 45$ cells from three animals per genotype at the age of P30. Statistics: ANOVA followed by Sidak's *post hoc* test. $^{*}p < 0.05$, $^{**}p < 0.01$, $^{***}p < 0.001$. ns = not significant.

Mir-183/96^{dko} synapses as compared with wt synapses. To account for a possible overestimation of co-localized GluA1 and Homer 1 puncta because of enlarged Homer 1 area in *Mir-183/96*^{dko} synapses, we normalized the number of co-localized GluA1 puncta to the total Homer 1 area. We still found more GluA1 puncta co-localized to Homer 1 in the normalized data (Fig. 8*F*; Table 4). Of note, Homer 1 is localized to the deeper layers of the PSD and neither binds AMPARs nor determines PSD size (e.g., Shiraishi-Yamaguchi and Furuichi, 2007; Sheng and Kim, 2011). This is in agreement with our ultrastructural data that did not show evidence for larger PSDs.

The fact that Homer 1 is likely not a good marker to study localization of AMPARs at the postsynaptic plasma membrane and represents itself a target of miR-96 let us decide to take an alternative approach. To determine the number of GluA1 puncta

Table 4. Analysis of presynaptic and postsynaptic structural components at the calyx of Held

Parameter	WT	KO	*p* value	Cohens *d*
Synaptic morphology				
n	45	45		
Number of SV2 clusters (puncta/100 μm^2)	41.55 ± 2.6	41.76 ± 2.96	0.96	
Area of SV2 clusters (μm^2)	7.98 ± 0.58	7.16 ± 0.56	0.32	
Relative SV2 immunoreactivity	3.56 ± 0.11	3.54 ± 0.13	0.92	
AZ composition				
n	45	45		
Number Bassoon clusters (particles/100 μm^2)	*Mir-183/96* ^{wt}: 38.19 ± 2.29	*Mir-183/96*^{dko}: 32.44 ± 2.10	0.067	
	Cldn14^{wt}: 40.28 ± 2.30	*Cldn14*^{ko}: 34.37 ± 2.75	0.11	
Size Bassoon clusters (μm^2)	*Mir-183/96* ^{wt}: 0.046 ± 0.0024	*Mir-183/96*^{dko} 0.056 ± 0.0022	0.0022	0.683
	Cldn14^{wt}: 0.044 ± 0.0014	*Cldn14*^{ko}: 0.048 ± 0.0019	0.26	
		Mir-183/96^{dko} vs. *Cldn14*^{ko}	0.0238	0.555
Relative Bassoon immunoreactivity	*Mir-183/96* ^{wt}: 4.85 ± 0.17	*Mir-183/96*^{dko}: 4.89 ± 0.15	0.85	
	Cldn14^{wt}: 5.50 ± 0.15	*Cldn14*^{ko}: 5.40 ± 0.21	0.73	
Number Piccolo clusters (particles/100 μm^2)	*Mir-183/96* ^{wt}: 28.81 ± 1.83	*Mir-183/96*^{dko}: 27.45 ± 1.67	0.56	
	Cldn14^{wt}: 37.18 ± 2.95	*Cldn14*^{ko}: 36.06 ± 2.03	0.77	
Size Piccolo clusters (μm^2)	*Mir-183/96* ^{wt}: 0.062 ± 0.0025	*Mir-183/96*^{dko}: 0.080 ± 0.0028	<0.0001	1.023
	Cldn14^{wt}: 0.054 ± 0.0016	*Cldn14*^{ko}: 0.061 ± 0.0020	0.13	
		Mir-183/96^{dko} vs. *Cldn14*^{ko}	<0.0001	1.173
Relative Piccolo immunoreactivity	*Mir-183/96* ^{wt}: 4.13 ± 0.11	*Mir-183/96*^{dko}: 4.63 ± 0.12	0.02	0.693
	Cldn14^{wt}: 4.39 ± 0.13	*Cldn14*^{ko}: 4.27 ± 0.16	0.57	
AZ ultrastructure				
n	36–41	31–25	0.349	
AZ length (nm)	343 ± 10	358 ± 12	0.586	
SV diameter (nm)	38 ± 0.4	38 ± 0.7	0.0029	0.809
Rel. fraction SVs within 20 nm	0.058 ± 0.004	0.089 ± 0.008	0.012	0.675
Number SVs within 20 nm/AZ	0.766 ± 0.06	1.012 ± 0.074		
GluA1 puncta				
n	45	45		
Number (puncta/100 μm^2)	*Mir-183/96* ^{wt}: 15.15 ± 1.19	*Mir-183/96*^{dko}: 27.78 ± 1.39	<0.0001	−3.92
	Cldn14^{wt}: 6.92 ± 0.86	*Cldn14*^{ko}: 10.89 ± 0.98	0.12	
		Mir-183/96^{dko} vs. *Cldn14*^{ko}	<0.0001	2.741
Size (μm^2)	*Mir-183/96* ^{wt}: 0.026 ± 0.00084	*Mir-183/96*^{dko}: 0.041 ± 0.0024	<0.0001	1.263
	Cldn14^{wt}: 0.024 ± 0.00073	*Cldn14*^{ko}: 0.021 ± 0.00074	0.59	
		Mir-183/96^{dko} vs. *Cldn14*^{ko}	<0.0001	1.572
Homer puncta				
n	30	30		
cumulative Homer1 area (μm^2)	31.11 ± 3.03	47.67 ± 2.71	<0.0001	−1.061
Synaptic GluA1				
n	30–45	30–45		
Co-localization with Homer1 (puncta/Homer area)	0.439 ± 0.053	0.939 ± 0.131	0.0009	−0.919
Co-localization with Piccolo (puncta/100 μm^2)	*Mir-183/96* ^{wt}: 13.82 ± 1.31	*Mir-183/96*^{dko}: 21.61 ± 1.52	0.0017	0.8
	Cldn14^{wt}: 20.08 ± 1.76	*Cldn14*^{ko}: 24.21 ± 1.67	0.19	

Data are shown as mean ± SEM.

that are indeed positioned synaptically, we examined the localization of GluA1 puncta in opposition to the AZ, delineated by the presynaptic protein Piccolo. We performed co-labeling of GluA1 and Piccolo and defined those GluA1 puncta as postsynaptically localized that overlapped at least 1% with Piccolo immunoreactivity in maximum intensity projections of small confocal image stacks (Fig. 8*G*,*H*). We refer to these particles as "synaptic GluA1." GluA1 was significantly elevated at the PSD of *Mir-183/96*^{dko} MNTB neurons as the number of synaptic GluA1 puncta increased by ~50% (Fig. 8*H*; Table 4). Importantly, this increase in synaptic GluA1 was not caused by homoeostatic upregulation of GluA1 because of peripheral deafness, since we did not observe significant differences in synaptic GluA1 in *Cldn14*^{ko} synapses (Table 4). Notably, number of synaptic puncta in this mouse line on a NMRI background seems to be generally on a higher level as compared with C57BL/6N mice. Taken together, these data reveal an increase in postsynaptic GluA1 subunits that are incorporated into the AMPAR complexes in the PSD of *Mir-183/96*^{dko} MNTB neurons. This increase at least partially explains the higher amplitudes of sEPSCs and eEPSCs in *Mir-183/96*^{dko} animals and reveals a role for miR-183/96 in the regulation of synaptic strength, both presynaptically and postsynaptically.

Discussion

The key finding of our study is that miR-183 and miR-96 are critical for presynaptic and postsynaptic regulation of synaptic strength. Their concomitant loss resulted in enormous EPSC amplitudes because of increased numbers of SVs released per AP, fueled by an enlarged RRP, and supported by increased GluA1 abundance at the PSD.

Regulation of synaptic transmission at the calyx of Held by miR-183/96

The dominating presynaptic effect of miR-183/96 loss is the increase in quantal content resulting in enormous EPSC

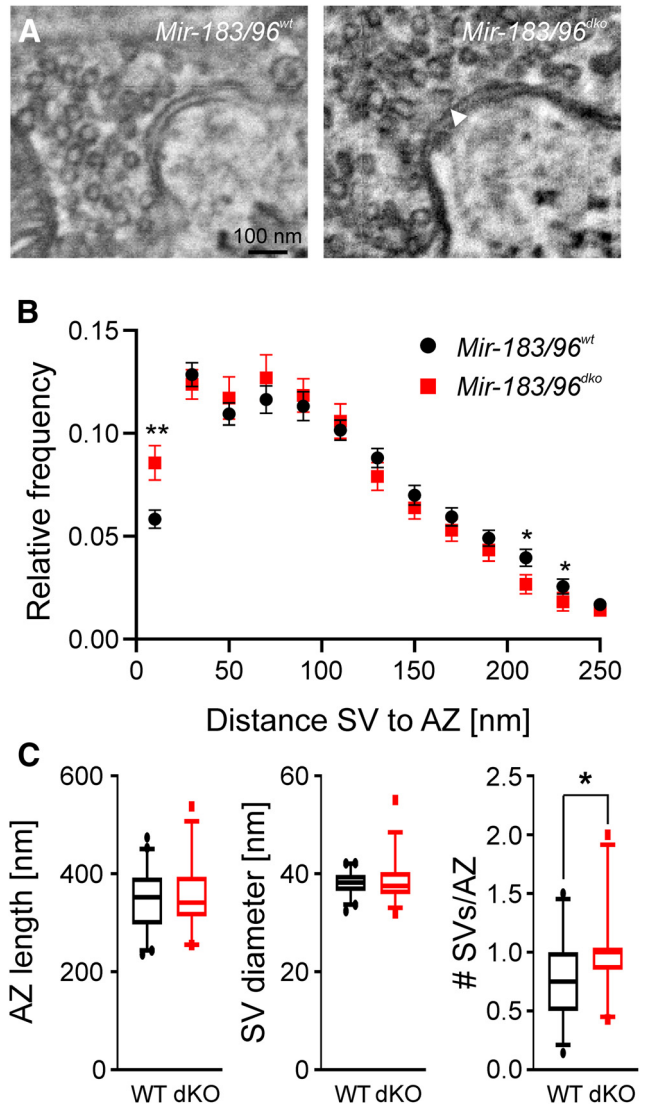

Figure 7. SV distribution is altered at AZ of *Mir-183/96*^{dko} calyces. ***A***, Representative electron micrographs of AZs from wt and *Mir-183/96*^{dko} calyces. The white arrowhead points to a SV close to the AZ (<20 nm). ***B***, Distribution of SV to AZ distances at AZs from wt and *Mir-183/96*^{dko} calyces. $N = 36$ (wt), 25 (dko) cells from three animals per genotype, #AZ/genotype ≥150. Statistics: Student's *t* test. ***C***, Quantification of PSD length (equal to AZ length), SV diameter, and average number of SVs close (<20 nm) to the AZ in wt and *Mir-183/96*^{dko} calyces. $N = 41$ (wt), 31 (dko) cells for PSD length and SV diameter and $N = 36$ (wt), 25 (dko) cells for #SVs/AZ. Cells have been derived from three animals per genotype. #AZ/genotype ≥150. Statistics: Student's *t* test. $^{*}p < 0.05$, $^{**}p < 0.01$.

amplitudes. Since the RRP was increased in parallel, the probability of release stayed constant in *Mir-183/96*^{dko} mice, suggesting that synaptic parameters related to the basic process of SV release like SNARE complex function and coupling to calcium channels are not affected by loss of miR-183/96. This is supported by the lack of changes in EPSC kinetics, STD and SV replenishment. The change in SV release without further alterations in kinetic parameters could come from an increase in AZ size, as the number of functional release sites scales with the size of the AZ (Holderith et al., 2012). The larger AZs could therefore provide space for a larger number of otherwise normal release sites. However, ultrastructural analysis revealed normal AZ diameter and area in *Mir-183/96*^{dko} calyces (area: ~10% increase assuming a circular AZ; Fig. 7*C*). Nevertheless, the analysis of SV-to-AZ distances revealed increased numbers of SVs in the immediate vicinity of AZ in *Mir-183/96*^{dko} calyces. This finding supports our electrophysiological data showing an increase in RRP size, since these membrane proximal SVs are thought to represent the RRP (Imig et al., 2014). Moreover, immunohistochemistry indicated increased amounts of Piccolo and Bassoon at the AZ and thus a change in the molecular composition of the AZ in *Mir-183/96*^{dko} synapses. Interestingly, neither Bassoon nor Piccolo have been implicated in the regulation of AZ and RRP size (Gundelfinger et al., 2015; Parthier et al., 2018). Their increased abundance at the AZ is hence likely caused indirectly by misregulation of yet unidentified miR-183/96 target(s).

Another striking effect of *Mir-183/96*^{dko} is the increased incorporation of GluA1 into synaptic AMPAR complexes of MNTB neurons. GluA1 has slower kinetics than GluA4 (Mosbacher et al., 1994) that normally dominate the calyx of Held synapse (Yang et al., 2011). However, juvenile MNTB neurons express GluA1 and switch to predominantly GluA4-containing AMPAR complexes around hearing-onset (Caicedo and Eybalin, 1999; Joshi et al., 2004; Koike-Tani et al., 2005; Lesperance et al., 2020) to support ultrafast synaptic transmission (Borst and van Soria Hoeve, 2012). We would like to emphasize that EPSCs in *Mir-183/96*^{dko} calyces are most likely still carried mainly by GluA4 containing AMPARs, as suggested by the unaltered, fast EPSC decay kinetics. The increased incorporation of GluA1 could take place either as homomeric GluA1 receptors or heteromeric GluA1/4 AMPARs, both of which differ in their regulation and biophysical properties. Since GluA1 is much more sensitive for glutamate than GluA4 (Traynelis et al., 2010), its incorporation into heteromeric GluA1/4 AMPARs could result in more AMPARs opening in response to SV fusion and glutamate release and thus explain at least partially the increased EPSC amplitude in response to AP-induced synchronous release.

Volume reduction of auditory brainstem nuclei in *mir-183/96*^{dko} mice

The volumes of both second (VCN) and third order auditory nuclei (LSO, MNTB) were reduced at P25–P27 and P60. As most of these changes are not caused by a lack of neuronal input because of deafness (Seal et al., 2008; Nothwang et al., 2015; Schlüter et al., 2018), proper auditory brainstem development seems to depend on on-site expression of miR-183/96. In addition, morphologic alterations were restricted to auditory nuclei as there were only subtle reductions in non-auditory regions. This confirms the requirement of *Mir-183/96* for proper development of sensory systems (Banks et al., 2020).

Of note, we observed a developmental difference between *Dmdo* and *Mir-183/96*^{dko} animals. In *Mir-183/96*^{dko} animals, volume and cell number were already reduced in the P0 MNTB. This points to a critical role of both miRs for proper embryonic development. In the *Dmdo* mouse, a smaller volume and cell loss was only observed at P4 (Schlüter et al., 2018). The embryonic requirement of miRNAs is in line with the loss of the entire SOC in mice lacking the miRNA processing enzyme Dicer (Rosengauer et al., 2012). The much milder phenotype in *Mir183/96*^{dko}, however, implicates roles for other miRNAs in embryonic development of the auditory hindbrain, too.

Genetic mechanisms underlying the observed phenotypes in *Dmdo* and *mir-183/96*^{dko} mice

We observed both overlapping and distinct phenotypes (e.g., increased NMDA/AMPA ratio and arrested fenestration of the calyx, respectively) between *Dmdo* and *Mir-183/96*^{dko} mice (Fig. 9*A*,*B*). At first glance, one might attribute the *Dmdo*-specific

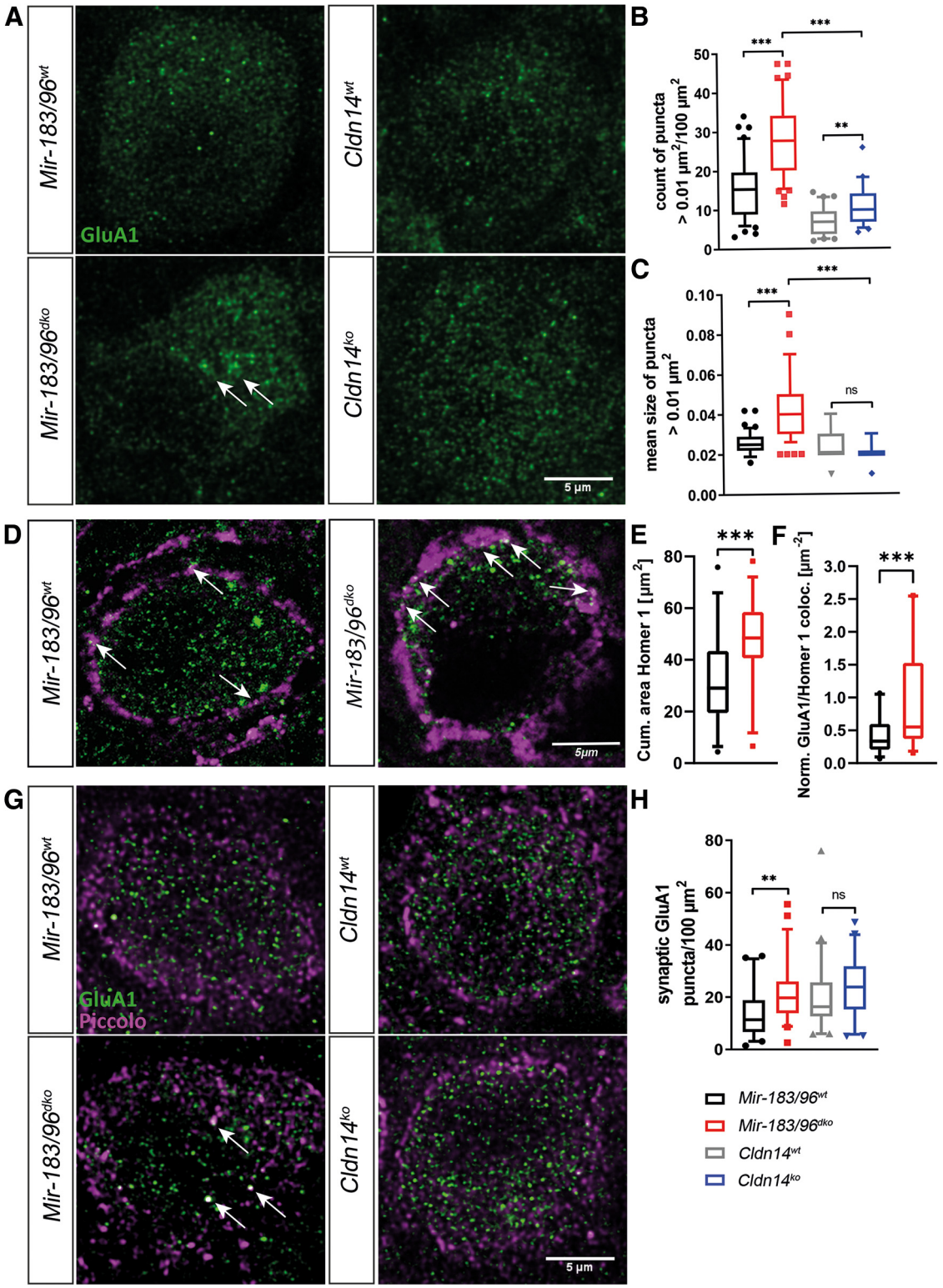

Figure 8. Increased number of larger GluA1 puncta and increased synaptic GluA1 in *Mir-183/96*^{dko} mice. ***A***, Representative images of MNTB principal cells after immunohistochemistry against GluA1 in in *Mir-183/96*^{dko} and corresponding wt mice and *Cldn14*^{ko} and corresponding wt mice. Arrows indicate larger GluA1 puncta in the *Mir-183/96*^{dko}. ***B***, ***C***, Quantification of the number (***B***) and size (***C***) of GluA1 puncta larger than 0.01 µm^2. $N = 45$ cells from three animals per genotype at the age of P30. Statistics: ANOVA followed by Sidak's *post hoc* test. ***D***, Representative MNTB principal cells after immunolabeling of GluA1 and the PSD protein Homer1 in *Mir-183/96*^{dko} and corresponding wt animals. ***E***, Quantification of the cumulative Homer1 area at the PSD of the calyx of Held. ***F***, Co-localization analysis of Homer1 and GluA1 puncta showing at least 1% overlap. The number of co-localized puncta was normalized to the cumulative Homer area, which was enlarged in *Mir-183/96*^{dko} mice. $N = 30$ cells from three animals per genotype at the age of P30. Statistics: Student's *t* test. ***G***, MNTB principal cells after immunohistochemistry against GluA1 (green, postsynaptic) and Piccolo (magenta, presynaptic AZs) in *miR-183/96* wt and dko and *Cldn14* wt and ko animals. Arrows indicate co-localized GluA1 and Piccolo signals showing larger GluA1 puncta that are located near the presynaptic AZs in the *Mir-183/96*^{dko} calyx. ***H***, Quantification of synaptic GluA1 showing at least 1% overlap with a Piccolo particle. $N = 45$ cells from three animals per genotype at the age of P30. Statistics: ANOVA followed by Sidak's *post hoc* test. All images represent maximal intensity projections of small confocal image stacks. $^{**}p < 0.01$, $^{***}p < 0.001$. ns = not significant.

A

Parameter	*Dmdo/Dmdo*	*Mir-183/96*^{dko}
Number of MNTB neurons	postnatally reduced	embryonically reduced
Cross section area of MNTB neurons	reduced	reduced
Fenestration	arrested	normal
Firing behavior	arrested switch from sustained to onset firing behavior	n.d.
K_v-immunoreactivity	reduced for Kv1.6 and BKβ2	n.d.
NMDA/AMPA ratio	increased	increased
Short term plasticity	unaltered at 100 Hz altered at 500 Hz	unaltered at 100 HZ n.d. at 500 Hz
mEPSCs/sEPSCs	increased	increased
eEPSC amplitude	unchanged	increased
Distribution of GluA1 subunit	n.d.	larger puncta
Distribution of Homer 1	n.d.	postsynaptically increased
Distribution of presynaptic active zone proteins piccolo/bassoon	n.d.	larger puncta
Readily releasable pool	lower	higher
Distribution of synaptic vesicles	n.d.	more SVs close to AZ (0-20 nm)

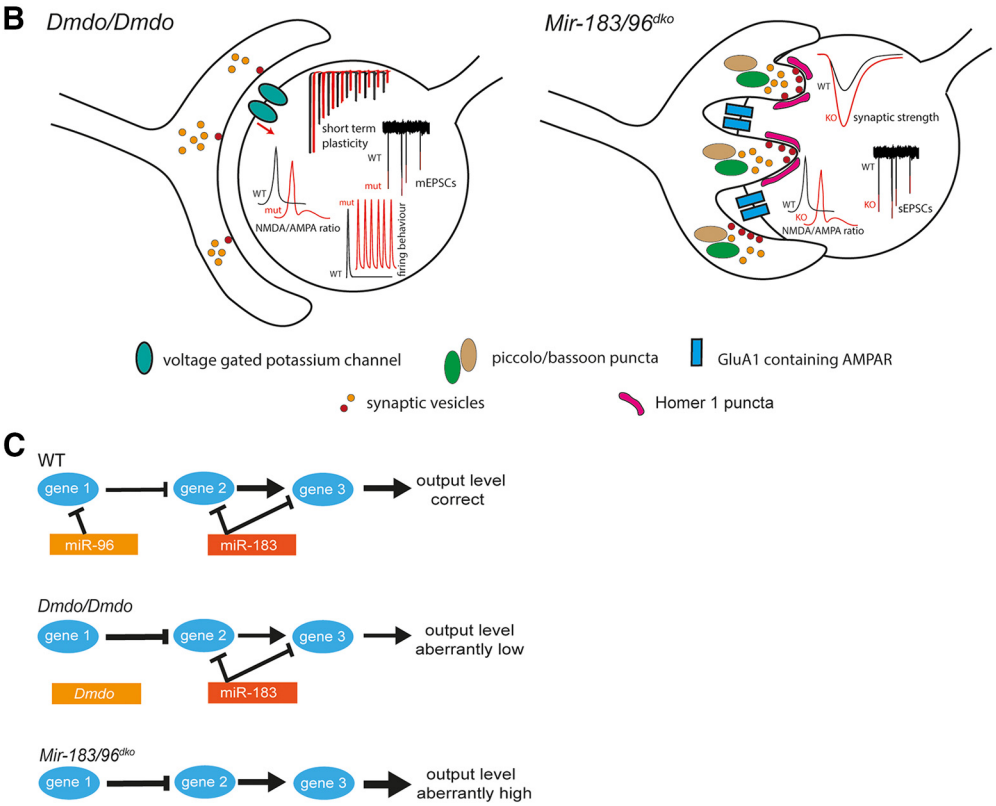

Figure 9. Comparison of the phenotypes observed in the *Dmdo* and *MiR-183/96*^{dko} mouse models. ***A***, ***B***, Morphologic features of the auditory hindbrain and physiological properties of the calyx of Held synapse are differentially altered in *Dmdo* mice harboring a point mutation in the miR96 (Schlüter et al., 2018) and in *MiR-183/96*^{dko} mice. However, some physiological properties (mEPSCs/sEPSCs, NMDA/AMA ratio) show the same phenotype in both mouse models. ***C***, Mechanistic model of the differential effects in the *Dmdo* and *Mir-183/96*^{dko} mouse model. The genomically clustered miRNAs might act on functionally linked genes. Arrows describe positive regulations, whereas vertical bars are standing for negative regulations. mEPSC, miniature excitatory postsynaptic current; sEPSC, spontaneous excitatory postsynaptic current.

alterations to a gain of new target genes, caused by the mutation in *Mir-96*. However, the developmental arrest observed in the cochlea of *Dmdo* mice likely represents, to a large degree, a loss of function, as the phenotype is shared between three distinct *Mir-96* mutations (Lewis et al., 2009; Mencía et al., 2009). It is highly unlikely that all three mutations recruit the same set of novel target genes (gain of function). A recent analysis suggests, however, an important contribution of novel targets from *MiR-96* point mutations (Lewis et al., 2021). In the auditory hindbrain, assignment of the *Dmdo*-specific phenotypes to a gain of function would also imply that the *Dmdo* mutation targets a master regulator of neuronal/sensory development. This is not

very likely, although we cannot formally exclude the possibility and some of the observed phenotypic changes such as altered expression of potassium channels likely reflect a gain of function as they are predicted targets of the mutated miR-96 only (Schlüter et al., 2018).

This raises the question, how a loss-of-function of miR-96 could result in different phenotypes in *Dmdo* and *Mir-183/96*^{dko} mice. Hints might come from their genomic organization. Genomically clustered miRNAs are co-transcribed with correlated expression levels of the mature miRNAs and frequently target different components of a protein network in a coordinate manner (Yuan et al., 2009; Hausser and Zavolan, 2014; Wang et al., 2016; Cantini et al., 2019). miR-183 and miR-96 are co-expressed in the auditory system from neonatal to adult stages (Pawlik et al., 2016; Krohs et al., 2021) and share six out of seven nucleotides in the seed region (Banks et al., 2020). This one mismatch and pronounced differences in the remainder sequence result in a limited overlap in predicted target genes (96 out of 1317 targets; Banks et al., 2020). A possible scenario is therefore that their regulatory actions take place simultaneously and interdependently on functionally connected genes. Their regulatory effects would hence depend on that of the other miRNAs and only their concerted regulation would result in the correct level of target gene expression (Fig. 9*C*). In such a scenario, the *Dmdo* mutation could result in a gene dose too low to start the fenestration process (Fig. 9*C*, middle panel), whereas a higher-than-normal output in *Mir-183/96*^{dko} (Fig. 9*C*, lower panel) would not affect fenestration. The differential regulation of RRP size in the two mouse models on the other hand would reflect a narrow optimal gene dose. The decrease observed in *Dmdo* calyces would again reflect impaired developmental upregulation, whereas the increase in *Mir-183/96*^{dko} synapses would result from a too high output because of the loss of regulation by both miRNAs. However, validation of this model has to await mice with targeted deletion of either of the miRNAs.

Physiologic roles of miR-183/96

Expression of both miRNAs persists into adulthood (Pawlik et al., 2016; Krohs et al., 2021) raising questions about their role in the mature auditory system. The calyx is optimized for robust, high-fidelity neurotransmission with no long-term synaptic plasticity (Leão, 2019). Although short-term plasticity has been extensively described *in vitro* (Borst and van Soria Hoeve, 2012; see above), its relevance *in vivo* is not clear (Lorteije et al., 2009). Our data do not suggest a role for either of the miRNAs in STD as it remains unaffected in *Mir-183/96*^{dko} synapses. Interestingly, long-term changes in the auditory environment such as noise rearing and conductive hearing loss change the properties of large, central auditory synapses in a reversible manner. The observed synaptic phenotypes include changes in release probability, the size of the RRP, VGluT1-cluster size, release site number, and synapse structure (Oleskevich and Walmsley, 2002; Grande et al., 2014; Ngodup et al., 2015; Clarkson et al., 2016). Additionally, on the postsynaptic site, alterations in the abundance of AMPAR subunits and EPSC amplitudes have been reported (Clarkson et al., 2016 and Oleskevich and Walmsley, 2002, respectively). These alterations at least partially resemble the effects observed here in *Mir-183/96*^{dko} synapses. It is thus tempting to speculate that miR-183/96 might participate in the regulation of long-term adaptions to the auditory environment.

In summary, we identified a genetic element involved in the regulation of synaptic strength both at the presynaptic and postsynaptic site of the calyx of Held. This makes miR-183/96 attractive candidates for coordinating developmental processes as well as adaptations in synaptic transmission in response to changes in auditory input.

References

Alles J, Fehlmann T, Fischer U, Backes C, Galata V, Minet M, Hart M, Abu-Halima M, Grässer FA, Lenhof HP, Keller A, Meese E (2019) An estimate of the total number of true human miRNAs. Nucleic Acids Res 47:3353–3364.

Banks SA, Pierce ML, Soukup GA (2020) Sensational microRNAs: neurosensory roles of the microRNA-183 family. Mol Neurobiol 57:358–371.

Bartel DP (2018) Metazoan microRNAs. Cell 173:20–51.

Ben-Yosef T, Belyantseva IA, Saunders TL, Hughes ED, Kawamoto K, Van Itallie CM, Beyer LA, Halsey K, Gardner DJ, Wilcox ER, Rasmussen J, Anderson JM, Dolan DF, Forge A, Raphael Y, Camper SA, Friedman TB (2003) Claudin 14 knockout mice, a model for autosomal recessive deafness DFNB29, are deaf due to cochlear hair cell degeneration. Hum Mol Genet 12:2049–2061.

Borst JGG, van Soria Hoeve J (2012) The calyx of Held synapse: from model synapse to auditory relay. Annu Rev Physiol 74:199–224.

Borst JG, Helmchen F, Sakmann B (1995) Pre- and postsynaptic whole-cell recordings in the medial nucleus of the trapezoid body of the rat. J Physiol 489:825–840.

Caicedo A, Eybalin M (1999) Glutamate receptor phenotypes in the auditory brainstem and mid-brain of the developing rat. Eur J Neurosci 11:51–74.

Cantini L, Bertoli G, Cava C, Dubois T, Zinovyev A, Caselle M, Castiglioni I, Barillot E, Martignetti L (2019) Identification of microRNA clusters cooperatively acting on epithelial to mesenchymal transition in triple negative breast cancer. Nucleic Acids Res 47:2205–2215.

Clarkson C, Antunes FM, Rubio ME (2016) Conductive hearing loss has long-lasting structural and molecular effects on presynaptic and postsynaptic structures of auditory nerve synapses in the cochlear nucleus. J Neurosci 36:10214–10227.

Dambal S, Shah M, Mihelich B, Nonn L (2015) The microRNA-183 cluster: the family that plays together stays together. Nucleic Acids Res 43:7173–7188.

Forsythe ID, Barnes-Davies M (1993) The binaural auditory pathway: excitatory amino acid receptors mediate dual timecourse excitatory postsynaptic currents in the rat medial nucleus of the trapezoid body. Proc R Soc Lond B 251:151–157.

Friedman RC, Farh KK-H, Burge CB, Bartel DP (2009) Most mammalian mRNAs are conserved targets of microRNAs. Genome Res 19:92–105.

Grande G, Negandhi J, Harrison RV, Wang L-Y (2014) Remodelling at the calyx of Held-MNTB synapse in mice developing with unilateral conductive hearing loss. J Physiol 592:1581–1600.

Gundelfinger ED, Reissner C, Garner CC (2015) Role of Bassoon and Piccolo in assembly and molecular organization of the active zone. Front Synaptic Neurosci 7:19.

Hausser J, Zavolan M (2014) Identification and consequences of miRNA-target interactions–beyond repression of gene expression. Nat Rev Genet 15:599–612.

Hirtz JJ, Boesen M, Braun N, Deitmer JW, Kramer F, Lohr C, Müller B, Nothwang HG, Striessnig J, Löhrke S, Friauf E (2011) Cav1.3 calcium channels are required for normal development of the auditory brainstem. J Neurosci 31:8280–8294.

Holderith N, Lorincz A, Katona G, Rózsa B, Kulik A, Watanabe M, Nusser Z (2012) Release probability of hippocampal glutamatergic terminals scales with the size of the active zone. Nat Neurosci 15:988–997.

Horstmann H, Körber C, Sätzler K, Aydin D, Kuner T (2012) Serial section scanning electron microscopy (S^3EM) on silicon wafers for ultra-structural volume imaging of cells and tissues. PLoS One 7:e35172.

Imig C, Min SW, Krinner S, Arancillo M, Rosenmund C, Südhof TC, Rhee J, Brose N, Cooper BH (2014) The morphological and molecular nature of synaptic vesicle priming at presynaptic active zones. Neuron 84:416–431.

Ishikawa T, Sahara Y, Takahashi T (2002) A single packet of transmitter does not saturate postsynaptic glutamate receptors. Neuron 34:613–621.

Jensen KP, Covault J (2011) Human miR-1271 is a miR-96 paralog with distinct non-conserved brain expression pattern. Nucleic Acids Res 39:701–711.

Joshi I, Wang LY (2002) Developmental profiles of glutamate receptors and synaptic transmission at a single synapse in the mouse auditory brainstem. J Physiol 540:861–873.

Joshi I, Shokralla S, Titis P, Wang LY (2004) The role of AMPA receptor gating in the development of high-fidelity neurotransmission at the calyx of Held synapse. J Neurosci 24:183–196.

Koike-Tani M, Saitoh N, Takahashi T (2005) Mechanisms underlying developmental speeding in AMPA-EPSC decay time at the calyx of Held. J Neurosci 25:199–207.

Körber C, Horstmann H, Venkataramani V, Herrmannsdörfer F, Kremer T, Kaiser M, Schwenger DB, Ahmed S, Dean C, Dresbach T, Kuner T (2015) Modulation of presynaptic release probability by the vertebrate-specific protein mover. Neuron 87:521–533.

Krohs C, Bordeynik-Cohen M, Messika-Gold N, Elkon R, Avraham KB, Nothwang HG (2021) Expression pattern of cochlear microRNAs in the mammalian auditory hindbrain. Cell Tissue Res 383:655–666.

Kuhn S, Johnson SL, Furness DN, Chen J, Ingham N, Hilton JM, Steffes G, Lewis MA, Zampini V, Hackney CM, Masetto S, Holley MC, Steel KP, Marcotti W (2011) miR-96 regulates the progression of differentiation in mammalian cochlear inner and outer hair cells. Proc Natl Acad Sci USA 108:2355–2360.

Leão RM (2019) The ion channels and synapses responsible for the physiological diversity of mammalian lower brainstem auditory neurons. Hear Res 376:33–46.

Lesperance LS, Yang YM, Wang LY (2020) Delayed expression of activity-dependent gating switch in synaptic AMPARs at a central synapse. Mol Brain 13:6.

Lewis BP, Shih IH, Jones-Rhoades MW, Bartel DP, Burge CB (2003) Prediction of mammalian microRNA targets. Cell 115:787–798.

Lewis MA, Quint E, Glazier AM, Fuchs H, Angelis MD, Langford C, van Dongen S, Abreu-Goodger C, Piipari M, Redshaw N, Dalmay T, Moreno-Pelayo MA, Enright AJ, Steel KP (2009) An ENU-induced mutation of miR-96 associated with progressive hearing loss in mice. Nat Genet 41:614–618.

Lewis MA, Buniello A, Hilton JM, Zhu F, Zhang WI, Evans S, van Dongen S, Enright AJ, Steel KP (2016) Exploring regulatory networks of miR-96 in the developing inner ear. Sci Rep 6:23363.

Lewis MA, Di Domenico F, Ingham NJ, Prosser HM, Steel KP (2021) Hearing impairment due to Mir183/96/182 mutations suggests both loss and gain of function effects. Dis Model Mech 14:dmm047225.

Lorteije JA, Rusu SI, Kushmerick C, Borst JG (2009) Reliability and precision of the mouse calyx of held synapse. J Neurosci 29:13770–13784.

Mencía A, Modamio-Høybjør S, Redshaw N, Morín M, Mayo-Merino F, Olavarrieta L, Aguirre LA, del Castillo I, Steel KP, Dalmay T, Moreno F, Moreno-Pelayo MA (2009) Mutations in the seed region of human miR-96 are responsible for nonsyndromic progressive hearing loss. Nat Genet 41:609–613.

Mosbacher J, Schoepfer R, Monyer H, Burnashev N, Seeburg PH, Ruppersberg JP (1994) A molecular determinant for submillisecond desensitization in glutamate receptors. Science 266:1059–1062.

Neher E, Sakaba T (2001) Combining deconvolution and noise analysis for the estimation of transmitter release rates at the calyx of Held. J Neurosci 21:444–461.

Ngodup T, Goetz JA, McGuire BC, Sun W, Lauer AM, Xu-Friedman MA (2015) Activity-dependent, homeostatic regulation of neurotransmitter release from auditory nerve fibers. Proc Natl Acad Sci USA 112:6479–6484.

Nothwang HG, Ebbers L, Schlüter T, Willaredt MA (2015) The emerging framework of mammalian auditory hindbrain development. Cell Tissue Res 361:33–48.

Oleskevich S, Walmsley B (2002) Synaptic transmission in the auditory brainstem of normal and congenitally deaf mice. J Physiol 540:447–455.

Parthier D, Kuner T, Körber C (2018) The presynaptic scaffolding protein Piccolo organizes the readily releasable pool at the calyx of Held. J Physiol 596:1485–1499.

Pawlik B, Schlüter T, Hartwich H, Breuel S, Heepmann L, Nothwang HG (2016) Comparative analysis of gene regulatory network components in the auditory hindbrain of mice and chicken. Brain Behav Evol 88:161–176.

Prosser HM, Koike-Yusa H, Cooper JD, Law FC, Bradley A (2011) A resource of vectors and ES cells for targeted deletion of microRNAs in mice. Nat Biotechnol 29:840–845.

Rosengauer E, Hartwich H, Hartmann AM, Rudnicki AM, Satheesh SV, Avraham KB, Nothwang HG (2012) Egr2::Cre mediated conditional ablation of Dicer disrupts histogenesis of mammalian central auditory nuclei. PLoS One 7:e49503.

Sätzler K, Söhl LF, Bollmann JH, Borst JGG, Frotscher M, Sakmann B, Lübke JHR (2002) Three-dimensional reconstruction of a calyx of Held and its postsynaptic principal neuron in the medial nucleus of the trapezoid body. J Neurosci 22:10567–10579.

Schlüter T, Berger C, Rosengauer E, Fieth P, Krohs C, Ushakov K, Steel KP, Avraham KB, Hartmann AK, Felmy F, Nothwang HG (2018) miR-96 is required for normal development of the auditory hindbrain. Hum Mol Genet 27:860–874.

Schneggenburger R, Meyer AC, Neher E (1999) Released fraction and total size of a pool of immediately available transmitter quanta at a calyx synapse. Neuron 23:399–409.

Seal RP, Akil O, Yi E, Weber CM, Grant L, Yoo J, Clause A, Kandler K, Noebels JL, Glowatzki E, Lustig LR, Edwards RH (2008) Sensorineural deafness and seizures in mice lacking vesicular glutamate transporter 3. Neuron 57:263–275.

Sheng M, Kim E (2011) The postsynaptic organization of synapses. Cold Spring Harb Perspect Biol 3:a005678.

Shiraishi-Yamaguchi Y, Furuichi T (2007) The Homer family proteins. Genome Biol 8:206.

Soldà G, Robusto M, Primignani P, Castorina P, Benzoni E, Cesarani A, Ambrosetti U, Asselta R, Duga S (2012) A novel mutation within the MIR96 gene causes non-syndromic inherited hearing loss in an Italian family by altering pre-miRNA processing. Hum Mol Genet 21:577–585.

Taschenberger H, von Gersdorff H (2000) Fine-tuning an auditory synapse for speed and fidelity: developmental changes in presynaptic waveform, EPSC kinetics, and synaptic plasticity. J Neurosci 20:9162–9173.

Taschenberger H, Leão RM, Rowland KC, Spirou GA, von Gersdorff H (2002) Optimizing synaptic architecture and efficiency for high-frequency transmission. Neuron 36:1127–1143.

Taschenberger H, Scheuss V, Neher E (2005) Release kinetics, quantal parameters and their modulation during short-term depression at a developing synapse in the rat CNS. J Physiol 568:513–537.

Toyoshima M, Sakurai K, Shimazaki K, Takeda Y, Shimoda Y, Watanabe K (2009) Deficiency of neural recognition molecule NB-2 affects the development of glutamatergic auditory pathways from the ventral cochlear nucleus to the superior olivary complex in mouse. Dev Biol 336:192–200.

Traynelis SF, Wollmuth LP, McBain CJ, Menniti FS, Vance KM, Ogden KK, Hansen KB, Yuan H, Myers SJ, Dingledine R (2010) Glutamate receptor ion channels: structure, regulation, and function. Pharmacol Rev 62:405–496.

Wang Y, Luo J, Zhang H, Lu J (2016) microRNAs in the same clusters evolve to coordinately regulate functionally related genes. Mol Biol Evol 33:2232–2247.

Xiao L, Michalski N, Kronander E, Gjoni E, Genoud C, Knott G, Schneggenburger R (2013) BMP signaling specifies the development of a large and fast CNS synapse. Nat Neurosci 16:856–864.

Yang YM, Aitoubah J, Lauer AM, Nuriya M, Takamiya K, Jia Z, May BJ, Huganir RL, Wang LY (2011) GluA4 is indispensable for driving fast neurotransmission across a high-fidelity central synapse. J Physiol 589:4209–4227.

Yuan X, Liu C, Yang P, He S, Liao Q, Kang S, Zhao Y (2009) Clustered microRNAs' coordination in regulating protein-protein interaction network. BMC Syst Biol 3:65.